On the role of optimal perturbations in the instability of monochromatic gravity waves

U. Achatz
Leibniz-Institut für Atmosphärenphysik an der Universität Rostock, 18225 Kühlungsborn, Germany

(Received 4 October 2004; accepted 19 July 2005; published online 21 September 2005)

Motivated by the useful new insights from optimal-perturbation theory into the onset of turbulence in other fields singular vectors (SVs) in stable and unstable gravity waves have been determined within the framework of the Boussinesq equations on an f plane. The difference between the dynamics of normal modes (NMs) and SV is characterized by a time invariance in the comparative role of the various possible exchange processes between NM and basic wave, while SV can have a highly time-dependent structure, allowing a more efficient energy exchange over a finite time. Both inertia-gravity waves (IGWs) and high-frequency gravity waves (HGWs) have been considered. At Reynolds numbers typical for the middle to upper mesosphere IGW admit rapid nonmodal growth even when no unstable NMs exist. SV energy growth within one Brunt-Vaisala period can cover two orders of magnitude, suggesting the possibility of turbulence onset under conditions where this would not be predicted by a NM analysis. HGWs show a dependence of short-term optimal growth on the direction of propagation of the perturbation with respect to the wave which is, at weak to moderate wave amplitudes, quite different from that of NM but reproduced in ensemble integrations from random initial perturbations. Their SVs are sharply peaked pulses with negligible group velocity which are repeatedly excited as the rapidly propagating wave passes over them. The transition of these to the leading NM, which is not moving with respect to the wave and which is typically broader in structure, is very slow, so that in many cases the turbulence onset via *local* perturbations of a gravity wave might be more appropriately described using optimal-perturbation theory. This might contribute to a better understanding of the often observed occurrence of thin turbulent layers in the middle atmosphere. © *2005 American Institute of Physics*.
[DOI: 10.1063/1.2046709]

I. INTRODUCTION

It is widely recognized that internal gravity waves play an important role in both oceanic and atmospheric dynamics.[1,2] In the atmosphere, they are typically excited in the troposphere (between the ground and about 10-km altitude). Due to energy conservation in a vertically decreasing ambient density field they gain in amplitude as they propagate upwards and thus become increasingly unstable.[3] The resulting wave breaking, possibly supplemented by critical-layer interactions,[4,5] leads to a deposition of momentum and energy which is essential for an understanding of the mean circulation in the mesosphere (about 50–90-km altitude). As a further consequence turbulence can be excited[6] which might be of relevance for the heat budget in the upper mesosphere.[7] While this overall picture is commonly agreed upon, many details in gravity-wave excitation, propagation, and finally breaking are not sufficiently understood yet, so that one is confronted with an uncomfortably large number of widely accepted, but quite different, schemes for the parametrization of the impact of gravity waves on the large-scale flow in the middle atmosphere.[6,8–12]

Many of the uncertainties are due to the lack of a simple picture of nonlinear gravity-wave breakdown. There is hope that direct numerical simulations will eventually help us in getting a better understanding of this complex process. Considerable progress has been made in this field,[13–20] but, also in view of the high demand such calculations put on presently available computer resources, good *a priori* knowledge of the developing scales and structures seems highly desirable. It thus appears important to have a very good understanding of the initial linear phase of the wave instability. It sets the stage for the nonlinear wave decay, and corresponding studies not only provide us with possible instability thresholds but also with perturbation patterns and wavelengths to be focused on in the simulations. Indeed much has already been learned in the past. A widespread misconception is that instability does not set in before the wave amplitude causes local vertical gradients of density (or potential temperature) and flow field allowing for convective or dynamic instability. In the former case, one needs overturning of density or potential-temperature layers, while in the latter case, the local Richardson number Ri must fall due to sufficient vertical shear below a certain threshold. This picture rests on the work of Howard[21] and Miles[22] who have shown that in plane-parallel vertically stratified flow $\mathrm{Ri}<1/4$ is a necessary condition for instability. In high-frequency gravity waves (HGWs) with slantwise phase propagation (i.e., at a nonvertical inclination angle to the horizontal) these studies are not applicable. Indeed we know by now that these waves show instabilities at all amplitudes, unless damped by viscosity.[23–28] As shown by Lombard and Riley[27] it is neither the wave-related shear nor the corresponding stratification

 © 2005 American Institute of Physics

Downloaded 03 Nov 2005 to 195.37.145.100. Redistribution subject to AIP license or copyright, see http://pof.aip.org/pof/copyright.jsp

which is solely responsible for the growth of linear normal modes (NMs), but a mixture of the two. The leading perturbations are found to often propagate obliquely with respect to the gravity wave so that the instability process is three dimensional right from the initial linear phase. Moreover, the whole depends considerably on the gravity-wave inclination angle. Finally, while in a nonrotating fluid all gravity waves are linearly polarized in their horizontal flow field, rotation causes their polarization to be increasingly circular as their direction of phase propagation changes from horizontal to vertical. The instability dynamics of nearly vertically propagating inertia-gravity waves (IGWs) in a rotating fluid is influenced by this. For IGW packets the linear instability has been examined in various investigations,[29–32] and a study for monochromatic IGW has been made by Yau *et al.*[33] At convectively unstable wave amplitudes, rapidly growing leading NMs are found, with a direction of propagation in the horizontal with respect to the IGW which changes from transverse to parallel as the gravity-wave inclination angle gets more and more vertical. However, as for gravity waves in a nonrotating fluid, obliquely propagating growing NMs are always found so that also the IGW breaking process is intrinsically three dimensional. At convectively stable amplitudes NM growth is, even in the inviscid-nondiffusive limit, rather weak, unless the IGW inclination angle is extremely steep.

Despite all the knowledge we have acquired on the linear stability problem there is an additional interesting aspect which is just beginning to get a systematic focus. Since the studies mentioned above use NM analyses, they provide information about possible time-asymptotic wave instabilities at infinitely small perturbation level. It is, however, known from several other fields that under conditions when no growing NMs exist rapid transient growth of so-called singular vectors (SVs) is often still possible.[34–38] Provided a sufficiently high, but possibly yet small, initial perturbation level is available this can lead to the onset of turbulence even when such a result would not be expected from a NM analysis. Moreover, even if growing NMs exist, it may happen that they take much longer in their amplification so that the incipient instability is better characterized by transient growth leading directly into the nonlinear decay phase. In two studies Achatz and Schmitz[39,40] (henceforth referred to as AS12) have examined the relevance of this concept for the IGW packet stability problem in the mesosphere. Indeed it is found that quite rapid growth of SVs occurs at wave amplitudes not permitting any NM to grow. This suggests a study on the relevance of SV for the general gravity-wave stability problem, i.e., for all inclination angles.

Such an investigation is described here. For greatest possible simplicity this study focuses on monochromatic waves, and indeed it will be seen that what has been found in AS12 on the linear dynamics of IGW packets is basically retrieved in this more simple scenario. The paper is structured as follows: Sec. II defines the gravity waves which are analyzed for their stability. Section III briefly reviews the linear stability theory for such waves and compares the concepts of NM and SV. In Sec. IV these are applied to the gravity-wave stability problem, and the growth intensity and dynamics of both types of perturbations are compared with each other. Section V contains a short analysis of the impact of Reynolds number and rotation on these results. Section VI gives an assessment of the relevance of optimal growth for the propagation of a gravity wave in a medium with random ambient fluctuations. Finally everything is summarized and discussed in Sec. VII.

II. GRAVITY WAVES IN A ROTATING BOUSSINESQ FLUID

The stability problem is discussed in the simplest possible framework, i.e., the Boussinesq equations on an f plane

$$\nabla \cdot \mathbf{v} = 0, \tag{1}$$

$$\frac{\partial \mathbf{v}}{\partial t} + (\mathbf{v}\cdot\nabla)\mathbf{v} + f\mathbf{e}_z \times \mathbf{v} + \nabla p - \mathbf{e}_z b = \nu\nabla^2\mathbf{v}, \tag{2}$$

$$\frac{\partial b}{\partial t} + (\mathbf{v}\cdot\nabla)b + N^2 w = \mu\nabla^2 b. \tag{3}$$

Here $\mathbf{v}=(u,v,w)$ denotes the three-dimensional velocity field. The buoyancy $b=g[\theta-\bar{\theta}(z)]/\theta_0$ is a measure of the deviation of the potential temperature θ from a merely vertically dependent reference profile $\bar{\theta}(z)$, normalized by a characteristic value θ_0. g is the vertical gravitational acceleration. The squared background Brunt-Vaisala frequency is $N^2=(g/\theta_0)d\bar{\theta}/dz$. An equivalent interpretation of buoyancy and Brunt-Vaisala frequency is $b=-g[\rho-\bar{\rho}(z)]/\rho_0$ and $N^2=-(g/\rho_0)d\bar{\rho}/dz$, where ρ, $\bar{\rho}(z)$, and ρ_0 are density, a corresponding reference field, and a characteristic value, respectively. p is the pressure field, normalized by a constant reference density, f the Coriolis parameter, and $\mathbf{e}_z$ the vertical unit vector. The Boussinesq equations can be expected to give a reasonably good approximation of the full gravity-wave dynamics as long as the focus is on the processes with vertical scales of the order or less than the atmospheric or oceanic scale height. This is the case throughout this study. For viscosity and thermal diffusivity the typical upper-mesospheric values $\nu=\mu=1\ \mathrm{m}^2/\mathrm{s}$ are taken (unless stated otherwise). The f plane is located at 70° latitude. The Brunt-Vaisala frequency is $N=2\times10^{-2}\ s^{-1}$. For better readability for a broader audience it has been decided not to nondimensionalize the equations. One should, however, keep in mind that a nondimensionalization, using the gravity-wave wavelength Λ (specified below) and the Brunt-Vaisala period $T=2\pi/N$ as length and time scales, would leave as the only controlling parameters the ratio f/N, the Reynolds number $\mathrm{Re}=\Lambda^2/(\nu T)$, and the Prandtl number $\mathrm{Pr}=\nu/\mu$. For later reference also the energy density $e=1/2(|\mathbf{v}|^2+b^2/N^2)$ is introduced which obeys

$$\frac{\partial e}{\partial t} + \nabla\cdot\left[\mathbf{v}(e+p) - \nu\nabla\frac{|\mathbf{v}|^2}{2} - \mu\nabla\frac{b^2}{2N^2}\right] = -\nu\sum_{i=1}^{3}|\nabla v_i|^2 - \mu\left|\nabla\frac{b}{N}\right|^2. \tag{4}$$

In the inviscid-nondiffusive limit with typical (e.g., periodic)

Downloaded 03 Nov 2005 to 195.37.145.100. Redistribution subject to AIP license or copyright, see http://pof.aip.org/pof/copyright.jsp

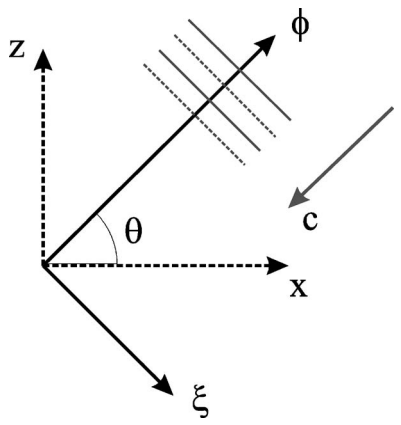

FIG. 1. The rotated and translated coordinate systems for the simplest representation of a gravity wave. The (orthogonal) ξ and ϕ axes lie in the x-z plane. The y axis points vertically into that plane. The new coordinate system moves with the phase velocity $\mathbf{c}$ of the gravity wave, rendering the latter stationary.

boundary conditions the volume integral of energy density is obviously a conserved quantity.

The equations admit as exact solutions monochromatic gravity waves of the form

$$\begin{pmatrix} \mathbf{v} \\ b \end{pmatrix} = \Re\left[\begin{pmatrix} \tilde{\mathbf{v}} \\ \tilde{b} \end{pmatrix} e^{i\phi} \right]. \tag{5}$$

The amplitudes $(\tilde{\mathbf{v}}, \tilde{b})$ will be specified below. The phase is $\phi = \mathbf{K}\cdot\mathbf{x} - \Omega t$, with wavenumber $\mathbf{K} = (k, l, m)$ and frequency Ω satisfying the dispersion relation

$$\Omega = \pm\sqrt{N^2 \cos^2\Theta + f^2 \sin^2\Theta}. \tag{6}$$

Here Θ is the inclination angle of the gravity-wave vector with respect to the horizontal so that $(\cos\Theta, \sin\Theta) = (k/\sqrt{k^2+m^2}, m/\sqrt{k^2+m^2})$. Without loss of generality it is assumed that $l=0$. At $m>0$ the—branch of the dispersion relation represents a wave with upward directed group velocity $\mathbf{c}_g = \nabla_{\mathbf{k}}\Omega$, but downward directed phase velocity $\mathbf{c} = (\Omega/K)(\mathbf{K}/K)$, where $K = |\mathbf{K}|$. This is the wave examined in the present study. Following Mied[23] and Drazin[41] a coordinate system is introduced in which the representation of the gravity wave is especially simple. It is obtained by a rotation about the y axis so that the new vertical coordinate points in the direction of the wavenumber vector, a translation along this axis with the phase velocity and a rescaling of the vertical axis in units of the wave phase (see also Fig. 1). The new coordinates are (ξ, y, ϕ) with

$$\xi = x\sin\Theta - z\cos\Theta, \tag{7}$$

$$\phi = K(x\cos\Theta + z\sin\Theta) - \Omega t. \tag{8}$$

The rotated velocity components along the new axes being u_ξ, v, and u_ϕ, the gravity wave takes in this representation the time-independent form

$$u_\xi = -a\frac{\Omega/K}{\sin\Theta\cos\Theta}\sin\phi, \tag{9}$$

$$v = a\frac{f/K}{\cos\Theta}\cos\phi, \tag{10}$$

$$u_\phi = 0, \tag{11}$$

$$b = -a\frac{N^2/K}{\sin\Theta}\cos\phi. \tag{12}$$

For easier comparability to some of the literature[24,33] we note that there the nondimensional u_ξ amplitude $2A = -(a\Omega/N)/(\sin\Theta\cos\Theta)$ is used for a characterization of the wave. The phase convention (following Yau *et al.*[33]) is such that the buoyancy gradient minimizes (maximizes) at ϕ

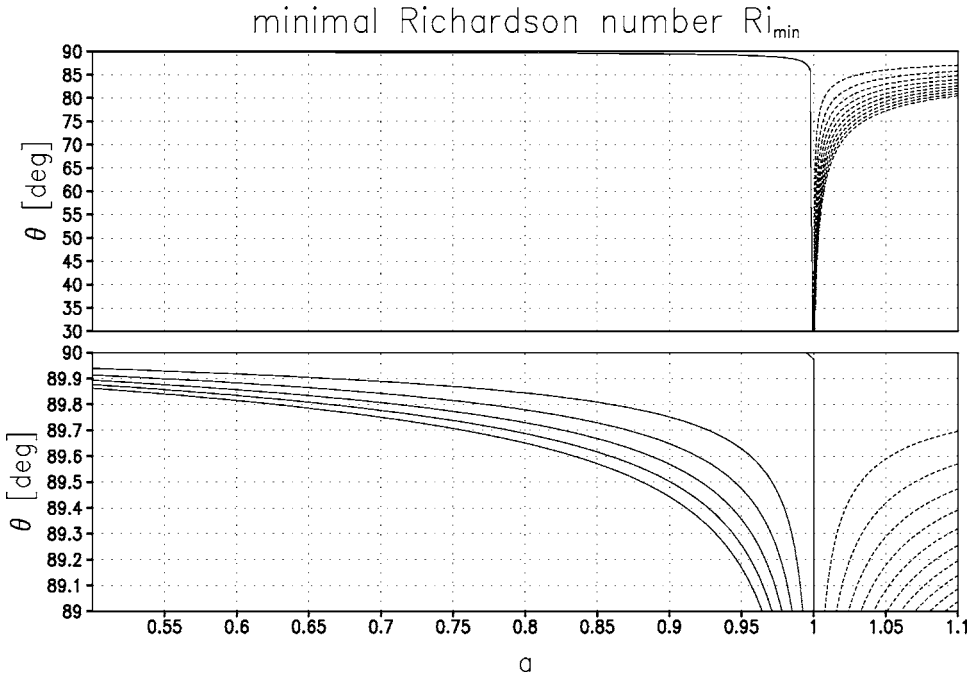

FIG. 2. The minimal Richardson number $\mathrm{Ri}_{\min}$ in a gravity wave in its dependence on the wave amplitude a with respect to the convective instability and its inclination angle Θ with respect to the horizontal. The upper panel shows the range of $30° \leqslant \Theta \leqslant 90°$. The isolines are between 0.25 (leftmost contour) and −50.25 in steps of 5. The lower panel shows the range of $89° \leqslant \Theta \leqslant 90°$. Here the contours are between 0.25 and −0.5 in steps of 0.05.

Downloaded 03 Nov 2005 to 195.37.145.100. Redistribution subject to AIP license or copyright, see http://pof.aip.org/pof/copyright.jsp

$=3\pi/2(\pi/2)$. The largest shear due to u_ξ occurs at $\phi=0,\pi$, and the largest shear due to v (only relevant for IGW where $R=|f/\Omega|$ is not negligible) is at the extrema of the buoyancy gradient. The nondimensional amplitude a is defined so that the wave is statically stable for $a<1$, i.e., at these values one has $N^2+\partial b/\partial z>0$ everywhere. In other words it is the amplitude relative to the overturning or static instability threshold. Its relationship to the amplitude of u_ξ and to energy density integrated over one wave train is given by

$$E=\int_0^{2\pi} d\phi e=\pi\frac{a^2(f^2\sin^2\Theta+N^2\cos^2\Theta)}{K^2\sin^2\Theta\cos^2\Theta}=\pi\left(2A\frac{N}{K}\right)^2. \tag{13}$$

In view of its frequent application, the local Richardson number in the wave also deserves a short discussion. It appears in a NM analysis of a shear flow obtained by neglecting in the gravity wave all vertical motions, its time dependence, and the horizontal dependence. The resulting Taylor-Goldstein equation[21,22,31,42] contains a height-dependent Richardson number which also depends on the horizontal direction of propagation of the NM with respect to that of the gravity wave. A necessary condition for a NM to grow is that its respective Richardson number is less than 1/4 anywhere.[21,22] Of most interest therefore is the minimum of the Richardson number, both over all horizontal directions of mode propagation and over all altitudes (or phases). At a given phase, the minimum over all directions of propagation is

$$\mathrm{Ri}_m=\frac{N^2+\partial b/\partial z}{(\partial u/\partial z)^2+(\partial v/\partial z)^2}. \tag{14}$$

Inserting the wave fields (9)–(12) and using the coordinate transformations (7) and (8) and the dispersion relation (6) one finds

$$\mathrm{Ri}_m=\frac{1-R^2}{a^2(1-\Omega^2/N^2)}\frac{1+a\sin\phi}{1-(1-R^2)\sin^2\phi}. \tag{15}$$

The minimum of Ri_m over all phases is at

$$\sin\phi=\begin{cases}-1 & \text{if } a>2(1-R^2)/(2-R^2)\\ -1/a+\sqrt{1/a^2-1/(1-R^2)} & \text{else.}\end{cases} \tag{16}$$

This minimal value $\mathrm{Ri}_{\min}$ is shown as a function of a and Θ in Fig. 2. As is well known, only for IGW the Richardson-number criterion $\mathrm{Ri}<0.25$ for dynamic instability can be satisfied for $a\ll 1$.

III. GRAVITY-WAVE INSTABILITY

A. The linear model

For the stability analysis the Boussinesq equations are linearized about the gravity-wave fields, henceforth denoted by $(\mathbf{V},B)$. Due to the symmetry of the problem in ξ and y different perturbation wavenumbers in the corresponding plane are not coupled by the linear equations. It therefore makes sense to use the ansatz[23,24,41] $(\hat{\mathbf{v}},\hat{b})=\Re\{(\mathbf{v},b)\times(\phi,t)\exp[i(\kappa\xi+\lambda y)]\}$ so that the componentwise equations in the rotated and translated coordinate systems become, with $\mathbf{v}=(u_\xi,v,u_\phi)$,

$$i\kappa u_\xi+i\lambda v+K\frac{\partial u_\phi}{\partial\phi}=0, \tag{17}$$

$$\frac{Du_\xi}{Dt}+Ku_\phi\frac{dU_\xi}{d\phi}+i\kappa p+b\cos\Theta-\sin\Theta fv=\nu\nabla^2u_\xi, \tag{18}$$

$$\frac{Dv}{Dt}+Ku_\phi\frac{dV}{d\phi}+i\lambda p+f(\sin\Theta u_\xi+\cos\Theta u_\phi)=\nu\nabla^2v, \tag{19}$$

$$\frac{Du_\phi}{Dt}+K\frac{\partial p}{\partial\phi}-b\sin\Theta-\cos\Theta fv=\nu\nabla^2u_\phi, \tag{20}$$

$$\frac{Db}{Dt}+Ku_\phi\frac{dB}{d\phi}+N^2(\sin\Theta u_\phi-\cos\Theta u_\xi)=\mu\nabla^2b, \tag{21}$$

using the shortcuts $D/Dt=\partial/\partial t-\Omega\partial/\partial\phi+i(\kappa U_\xi+\lambda V)$ and $\nabla^2=-(\kappa^2+\lambda^2)+K^2\partial^2/\partial\phi^2$.

Since the coefficients of Eqs. (17)–(21) are periodic in ϕ with period 2π, Floquet theory[27,43] tells us that it is possible to consider independently solutions of the form $(\mathbf{v},b)=\exp(i\eta\phi)(\mathbf{v}',b')(\phi,t)$ with $(\mathbf{v}',b')(\phi+2\pi,t)=(\mathbf{v}',b')\times(\phi,t)$ and $-1/2\leqslant\eta\leqslant 1/2$. In line with Lombard and Riley[27] the present analysis is restricted to $\eta=0$. At least for IGW Yau *et al.*[33] have shown that this generally captures the leading NM. Obvious respective generalizations are left to future studies.

For a numerical treatment (17)–(21) have been discretized on a standard staggered grid in ϕ (u_ξ, v, p, and b on full levels, and u_ϕ on intermediate half levels, see, e.g., Durran[44]) with periodic boundary conditions. The model domain extends from 0 to 2π. Pressure is obtained by applying the divergence on the momentum equations, using (17), and solving the resulting Poisson equation by a Fourier transform technique. Lining up the complex grid-point values of all model variables $(\mathbf{v},b)$ in one complex state vector $\mathbf{x}$ an abstract condensation of the model equations is $d\mathbf{x}/dt=\mathcal{A}\mathbf{x}$, with a model operator $\mathcal{A}$ depending on the basic wave and

Downloaded 03 Nov 2005 to 195.37.145.100. Redistribution subject to AIP license or copyright, see http://pof.aip.org/pof/copyright.jsp

on κ and λ. The time integration is done by two initial fourth-order Runge-Kutta time steps, followed by third-order Adams-Bashforth time steps.[44]

B. Normal modes

Once the linear equations have been discretized the corresponding NMs are simply defined as the eigenvectors $\mathbf{n}_\nu$ of the model operator, satisfying

$$\mathcal{A}\mathbf{n}_\nu = -i(\omega_\nu + i\gamma_\nu)\mathbf{n}_\nu \tag{22}$$

with an eigenvalue consisting of an eigenfrequency ω_ν and a growth rate γ_ν. An initial state given up to an amplitude a_ν by a NM, i.e., $\mathbf{x}(0)=a_\nu\mathbf{n}_\nu$, leads to a time-dependent solution

$$\mathbf{x}(t) = a_\nu e^{\gamma_\nu t} e^{i\omega_\nu t}\mathbf{n}_\nu, \tag{23}$$

so that the existence of a growing NM with $\gamma_\nu > 0$ implies linear instability. In addition, in typical cases where all NMs form together a complete set, every initial state can be written as a superposition of NM behaving in time as given by (23) so that, *if an initial state projects even to the least onto the leading NM (if there is one, with largest γ_ν), this NM will be approached asymptotically as $t\to\infty$.*

C. Singular vectors

While a NM analysis searches perturbations growing exponentially in time, a SV analysis explores the possibility of rapid *transient* growth. For this one needs a definition of the strength of a perturbation, i.e., a norm $\|\mathbf{x}\|^2=\bar{\mathbf{x}}^t\mathcal{M}\mathbf{x}$, where the metric $\mathcal{M}$ is positive definite and symmetric. The upper index t denotes transposition, the overbar taking the complex conjugate. Among the different possible choices the present study uses the discretized version of

$$\|\mathbf{x}\|^2 = \int_0^{2\pi} d\phi\varepsilon = \int_0^{2\pi} d\phi\frac{1}{2}\left(|\mathbf{v}|^2 + \frac{|b|^2}{N^2}\right), \tag{24}$$

with an integrand ε which is twice the average of energy density over one horizontal wavelength of the perturbation. The metric thus takes a simple diagonal form. Given a norm, a SV analysis asks what initial perturbation $\mathbf{x}(0)$ would maximize for some given finite time τ the ratio $\|\mathbf{x}(\tau)\|^2/\|\mathbf{x}(0)\|^2$. For an answer one needs the propagator matrix $\Phi(t)=\exp(\mathcal{A}t)$ mapping the initial perturbation to its state at $t=\tau$ via $\mathbf{x}(\tau)=\mathbf{\Phi}(\tau)\mathbf{x}(0)$. The variational analysis tells us that the desired perturbation initializing the strongest growth is the leading eigenvector $\mathbf{p}_\nu$ satisfying

$$\mathcal{M}^{-1}\bar{\mathbf{\Phi}}^t(\tau)\mathcal{M}\mathbf{\Phi}(\tau)\mathbf{p}_\nu = \sigma_\nu^2\mathbf{p}_\nu \tag{25}$$

with the largest possible eigenvalue σ_ν^2, which is the squared growth factor $\|\mathbf{x}(\tau)\|^2/\|\mathbf{x}(0)\|^2$ if $\mathbf{x}(0)=\mathbf{p}_\nu$. $\mathcal{M}$ being symmetric and positive definite there is a Cholesky factorization $\mathcal{M}=\bar{\mathcal{N}}^t\mathcal{N}$, where $\mathcal{N}$ is upper triangular (diagonal in our case). Inserting the factorization into (25) and defining $\mathbf{q}_\nu=\mathcal{N}\mathbf{p}_\nu$ the eigenvalue problem can be rewritten as $\bar{\mathcal{L}}^t\mathcal{L}\mathbf{q}_\nu=\sigma_\nu^2\mathbf{q}_\nu$ with $\mathcal{L}=\mathcal{N}\mathbf{\Phi}(\tau)\mathcal{N}^{-1}$, showing that all eigenvalues are positive. The eigenvectors $\mathbf{q}_\nu$ are orthogonal with respect to the Euclidean metric, and henceforth also the optimal perturbations $\mathbf{p}_\nu$ with respect to $\mathcal{M}$. The time-dependent state $\mathbf{\Phi}(\tau)\mathbf{p}_\nu$ developing from an optimal perturbation $\mathbf{p}_\nu$ is the corresponding SV.

NM and SV differ in several regards. So one observes that NMs always have the same oscillating structure which is simply growing or decaying in time. This is not the case for SV. Their structure can differ quite a lot between initialization and final time. As a consequence, the exchange processes between perturbation and background responsible for the change in amplitude are always the same for a NM, while they can vary considerably in the development of a SV. For a non-normal model operator (where $\bar{\mathcal{A}}^t\mathcal{A}\neq\mathcal{A}\bar{\mathcal{A}}^t$) it can also be shown that the leading SV and leading NM only agree as $\tau\to\infty$.

IV. A COMPARISON BETWEEN NORMAL MODES AND SINGULAR VECTORS FOR GRAVITY WAVES WITH DIFFERENT INCLINATION ANGLES

In the following a comparison is given between the NM and SV for typical gravity-wave scales. The wavelength of the gravity wave has been chosen to be $\Lambda=2\pi/K=6$ km, implying a Reynolds number $\mathrm{Re}=1.1\times10^5$. In comparing the results for different inclination angles a choice had to be made about how to treat the wave amplitude a with respect to convective instability. One option would be keeping a fixed. This, however, leads to infinite energy, and correspondingly infinite gradients, at $\Theta=0°$ and $\Theta=90°$. This study therefore follows Yau *et al.*[33] and keeps in comparisons between different inclination angles the amplitude in U_ξ (or equivalently the energy) fixed so that, using (13),

$$a(\Theta) = \frac{2A\sin\Theta}{\sqrt{1+(f/N)^2\tan^2\Theta}}. \tag{26}$$

For an overview of the effect of wave amplitude and inclination angle on the intensity of the respective NM and SV instabilities the study focuses on the representative inclination angles $\Theta=89.5°$, 70°, 50°, and 30°. This way an IGW is included ($\Theta=89.5°$) with not too extreme a value for R (0.62), as well as three HGW with periods $2\pi/\Omega=920$, 490, and 360 s. The examined amplitudes $A=0.45$, 0.55, and 0.76 have been chosen so that the IGW is either well below ($a=0.71$), slightly below ($a=0.87$), or above ($a=1.2$) the overturning threshold. For the reader's convenience the most important parameters of all examined waves are also listed in Table I.

As described above, a separate set of NM or SV belongs to each horizontal perturbation wave vector, which will in the following be defined by its wavelength $\lambda_\parallel$ (or wavenumber $k_\parallel=2\pi/\lambda_\parallel$), and the azimuthal angle α between wave vector and ξ axis, so that

$$(\kappa,\lambda) = \frac{2\pi}{\lambda_\parallel}(\cos\alpha,\sin\alpha). \tag{27}$$

In a complete analysis it is not necessary to survey the whole κ-λ plane. Due to the invariance of Eqs. (17)–(21) under the simultaneous transformations $(\kappa,\lambda)\to-(\kappa,\lambda)$ and complex conjugation $(\mathbf{v},b)\to(\bar{\mathbf{v}},\bar{b})$ it is sufficient to consider the subrange $0°\leqslant\alpha\leqslant180°$. In addition, in the absence of rotation, so that both f and V vanish, one would also have invariance

Downloaded 03 Nov 2005 to 195.37.145.100. Redistribution subject to AIP license or copyright, see http://pof.aip.org/pof/copyright.jsp

TABLE I. For all examined gravity waves, their inclination angle Θ with respect to the horizontal, their amplitude a with respect to the overturning threshold, the nondimensional amplitude A of the u_ξ wind, the ratio $R=f/|\Omega|$ between Coriolis parameter and wave frequency, and the smallest Richardson number in the whole phase range and among all directions of propagation of a perturbation, $\mathrm{Ri}_{\min}$.

Θ (°)	a	A	R	$\mathrm{Ri}_{\min}$
89.5	0.71	0.45	0.62	0.88
70	0.85	0.45	2.0×10^{-2}	1.2
50	0.69	0.45	1.1×10^{-2}	3.1
30	0.45	0.45	7.9×10^{-3}	19
89.5	0.87	0.55	0.62	0.28
70	1.0	0.55	2.0×10^{-2}	0
50	0.84	0.55	1.1×10^{-2}	1.9
30	0.55	0.55	7.9×10^{-3}	12
89.5	1.2	0.76	0.62	−0.23
70	1.4	0.76	2.0×10^{-2}	-5.8×10^{2}
50	1.2	0.76	1.1×10^{-2}	-2.1×10^{3}
30	0.76	0.76	7.9×10^{-3}	5.7

under the transformations $\lambda\rightarrow-\lambda$ and $v\rightarrow-v$. It turned out that, although this symmetry is broken by rotation, there is not much difference in the results between $\alpha=90°\pm\beta$. Therefore here only the subrange $0°\leqslant\alpha\leqslant90°$ is discussed.

For the practical determination of the leading NM and optimal perturbations (22) and (25) are solved, using an implicitly restarted Arnoldi method[45] and (for the optimal perturbations) the adjoint Boussinesq model extracted from the linear model with the help of the tangent and adjoint model compiler (TAMC).[46] Details are given in AS12. The number of grid points used in the model discretization, usually 1024, was always chosen so as to well resolve all relevant scales.

A. Growth factors

Since optimal growth should show the largest differences from NM behavior at short-optimization times this study mainly focuses on $\tau=300$ s, which is approximately one Brunt-Vaisala period. Longer-optimization times are discussed briefly in order to give a rough overview of the various possibilities.

Looking first at the *shorter-optimization time* $\tau=300$ s, Fig. 3 shows for $A=0.45$ the growth factors $\sigma_1=e^{\gamma_1\tau}$ of the leading NM of the four gravity waves, as a function of wavelength (or wavenumber) and azimuthal angle of the horizontal wavenumber vector of the mode. A glance at Table I shows that in none of the four cases an instability would have to be expected from an (inappropriate) application of the theory of Howard[21] and Miles.[22] Indeed the IGW case, best approaching the conditions examined by these authors, has no growing NM. It might be that in the inviscid-nondiffusive limit weak instabilities such as the ones published by Yau *et al.*[33] exist, but these seem to be damped by viscosity and diffusion. The other three cases are in agreement with previous findings on waves with slantwise phase propagation (e.g., Lombard and Riley[27]). All three examined gravity waves are unstable. While parallel perturbations (i.e., with $\alpha=0°$) grow most rapidly, there also is a second important azimuthal-angle range of $50°\leqslant\alpha\leqslant70°$. Moreover, the instability increases with decreasing inclination angle Θ.

A quite different picture is presented by the most rapidly growing SV. Their growth factors σ_1 are shown in Fig. 4. Although it has no unstable NM at all, even the IGW admits optimal growth by nearly a factor of 4. In agreement with the results in AS12 on IGW packets the most rapidly amplifying SVs propagate parallel to the IGW, but at a somewhat larger wavelength transverse perturbations ($\alpha=90°$) also amplify. From the NM analysis it does not come as a surprise that the three HGWs exhibit stronger instabilities. The ratio between

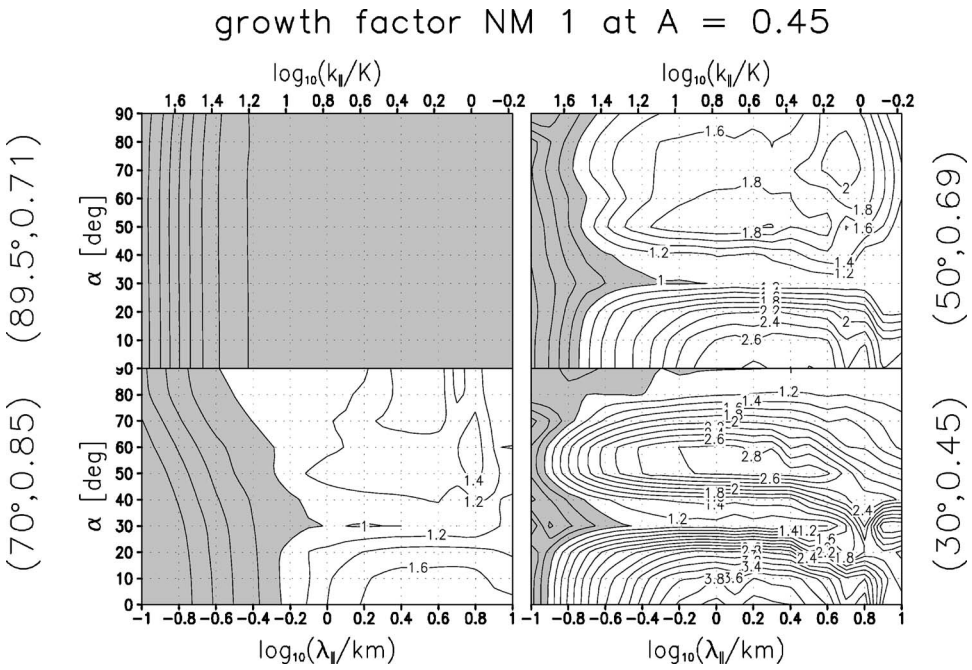

FIG. 3. The growth factors $\sigma_1=\exp(\gamma_1\tau)$ (integration time $\tau=300$ s) for the leading NM of four gravity waves with different inclination angles but identical energy or u_ξ amplitude (in nondimensional units $A=0.45$), as a function of the wavelength $\lambda_\parallel$ (or the corresponding wavenumber normalized by that if the basic wave, see the top axis), and the azimuthal angle α of the horizontal wave vector of the mode with respect to the ξ axis. The inclination angle and wave amplitude with respect to the convective overturning threshold of the four waves are $(\Theta,a)=(89.5°,0.71)$ (top-left panel), (70°,0.85) (bottom-left), (50°,0.69) (top-right), and (30°,0.45) (bottom-right). The contour interval is 0.2, values less than 1, i.e., the regions without NM growth, are indicated by shading. In the graph for $\Theta=89.5°$ the contour range is between 0.2 (leftmost contour) and 0.9 (rightmost) in steps of 0.1.

Downloaded 03 Nov 2005 to 195.37.145.100. Redistribution subject to AIP license or copyright, see http://pof.aip.org/pof/copyright.jsp

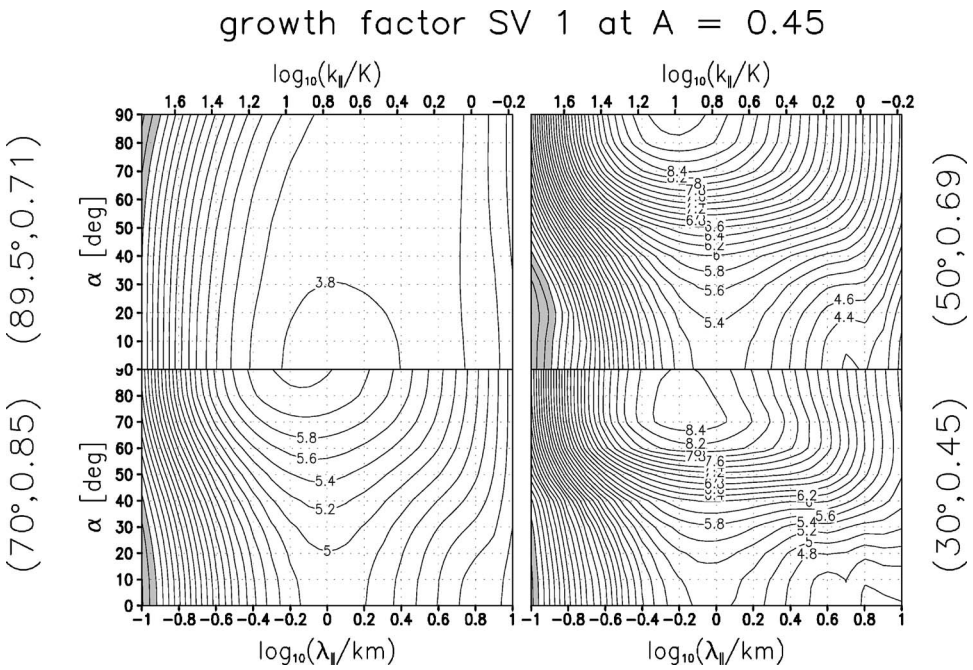

FIG. 4. As Fig. 3, but now the growth factors σ_1 of the leading SV. The contour interval is 0.2 everywhere.

optimal growth and growth of the leading NM increases with increasing inclination angle, ranging between 2 for $\Theta=30°$ and 4 for $\Theta=70°$. The most active wavelengths and azimuthal angles are quite different from those for the NM. In all HGW cases transverse instabilities are favored over parallel ones. At intermediate inclination angles they are the most rapid ones in the whole azimuthal-angle range, but for $\Theta=30°$ a propagation at $\alpha=70°$ with respect to the ξ axis is favored. Another difference is that here it is not the smallest inclination angle which leads to the strongest instability. The most rapid transient instabilities are found for $\Theta=50°$. Finally, the leading SVs tend to be at smaller wavelengths (between a few 100 m and 1 km) than the most unstable NMs which have scales more of the order of the wavelength of the basic wave.

Increasing the wave energy so that $A=0.55$, i.e., $a=0.87$ at $\Theta=89.5°$, leads to the NM and SV growth factors shown in Figs. 5 and 6. The main effect is to intensify the instabilities while leaving the favored scales and azimuthal angles the same. Still the IGW case shows no growing NM. Its optimal perturbations, however, amplify by nearly an order of magnitude. The growth-factor ratio between SV and NM for the HGW ranges between 2 at $\Theta=30°$ and 6 at $\Theta=70°$.

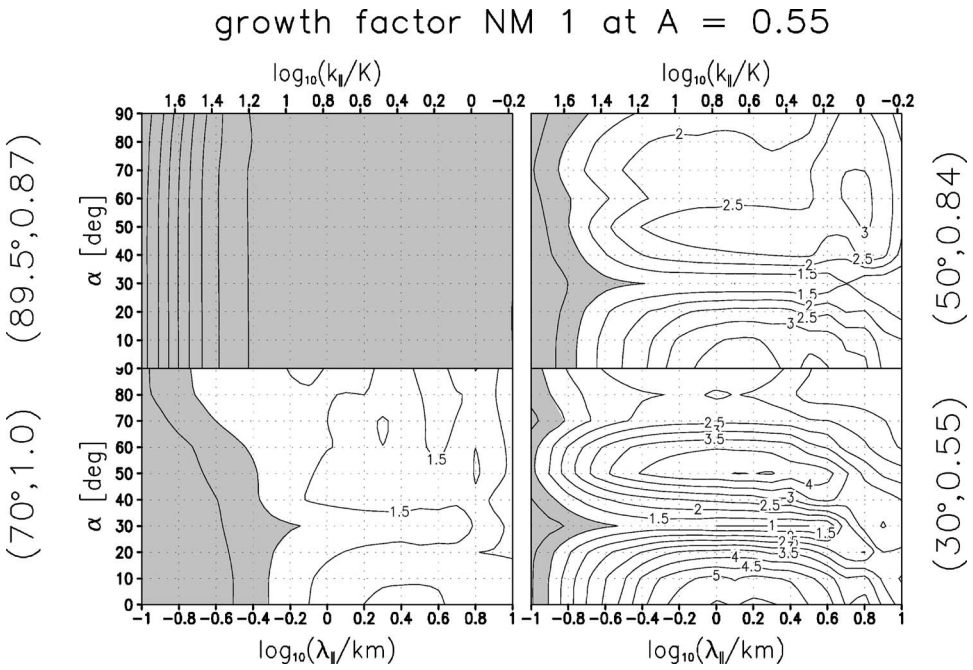

FIG. 5. As Fig. 3, but now with an increased wave energy so that $A=0.55$. For the IGW ($\Theta=89.5°$) the leftmost contour is at 0.2, the rightmost contour at 0.9, and the contour interval at 0.1. For the other cases the contour interval is 0.5.

Downloaded 03 Nov 2005 to 195.37.145.100. Redistribution subject to AIP license or copyright, see http://pof.aip.org/pof/copyright.jsp

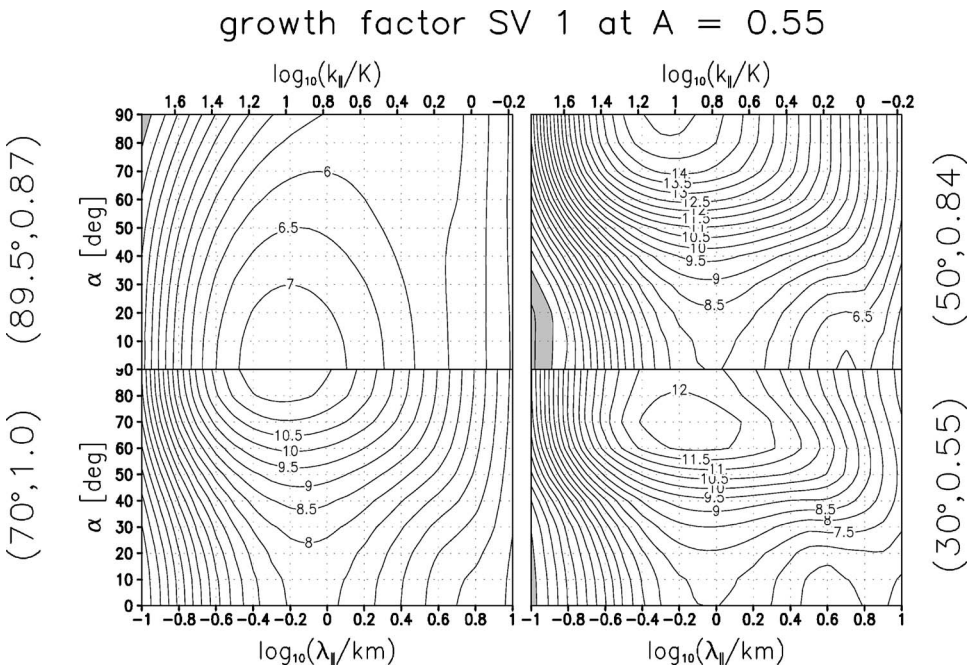

FIG. 6. As Fig. 5, but now for the leading SV.

An essential modification is caused by a further increase of the wave energy to a value of $A=0.76$, corresponding for the IGW to $a=1.2$. The growth factors for these cases can be seen in Figs. 7 and 8. As a consequence of considerable convective and dynamic instabilities the IGW now has unstable NM, as already shown by Dunkerton[31] and Yau *et al.*[33] The distribution of the instabilities over the α-$\lambda_\parallel$ plane is very similar to the one for optimal growth on the two IGWs with smaller amplitudes, favoring parallel propagation over a secondary maximum at transverse propagation. The SV growth factors for this IGW are, however, still larger than those for the NM by a factor of 5. In addition, the wavelengths of the leading SV are smaller than those of the most rapidly growing NM. With regard to the HGW, the NM growth maximum for $\Theta=70°$ now has shifted to transverse propagation, but at a wavelength which is about an order of magnitude larger than the one of the leading, also transverse, SV. In a comparison between the different inclination angles NM instability still is most intense at the smallest inclination angle $\Theta=30°$, although this is the only case not satisfying the instability criteria of Howard[21] and Miles[22] (see Table I). In contrast to the other two weaker wave amplitudes now, however, oblique propagation at $\alpha=50°$ is favored there over parallel propagation. For all inclination angles the optimal perturbations are found to amplify by more than an order of magnitude, with the most intense instability encountered at $\Theta=70°$. The growth-factor ratio between SV and NM ranges between 2.5 at $\Theta=30°$ and 10 at $\Theta=70°$.

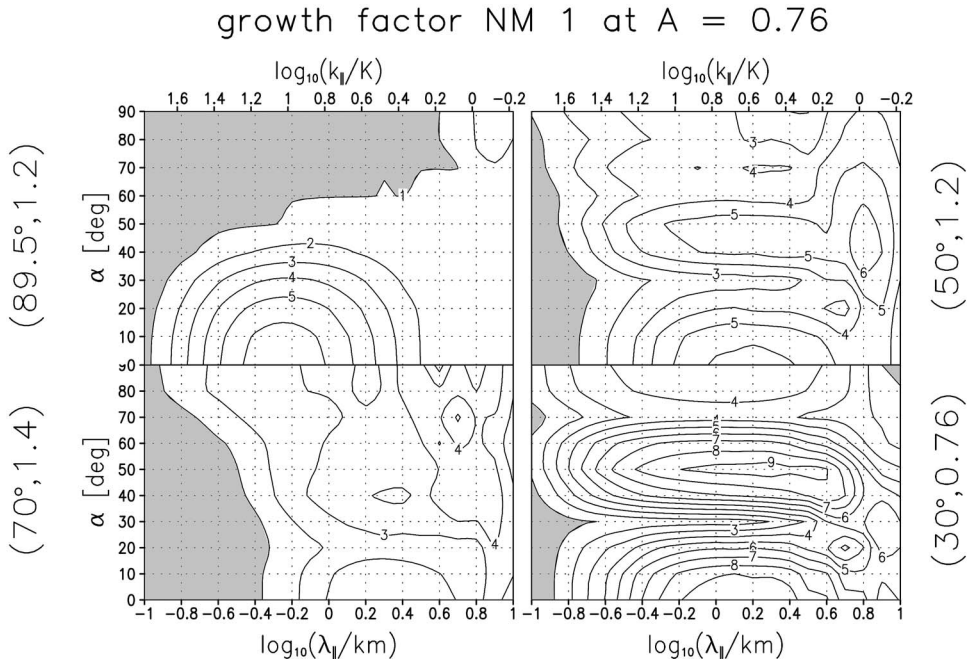

FIG. 7. As Fig. 3, but now with an increased wave energy so that $A=0.76$. The contour interval is 1.0 everywhere.

Downloaded 03 Nov 2005 to 195.37.145.100. Redistribution subject to AIP license or copyright, see http://pof.aip.org/pof/copyright.jsp

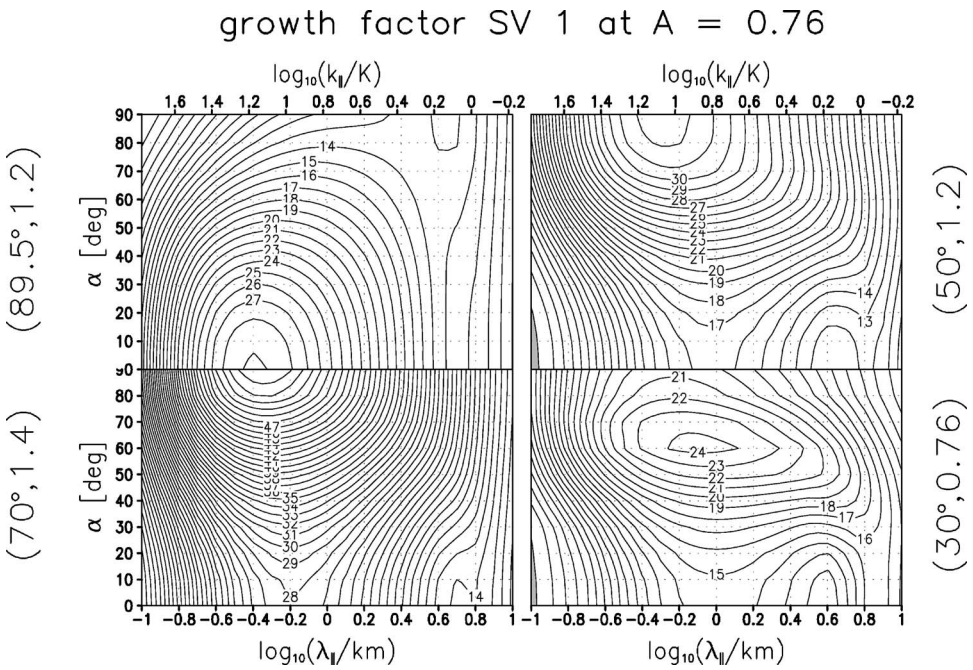

FIG. 8. As Fig. 7, but now for the leading SV.

For *longer-optimization times* one must distinguish between the two main cases where either growing NMs exist or not. In the latter case, one typically searches for the so-called global optimal, i.e., one attempts to find a value for τ where optimal growth maximizes. Such an analysis suggests itself for the subcritical ($a<1$) IGW examined here. In the former case nearly all initial perturbations eventually converge towards the set of leading NM so that within the linear approximation perturbation growth usually is not limited. This is the case for all HGWs examined here. Instead of searching for a global optimal it seems for these to be more meaningful to consider the longest time scale of dynamical relevance within the model framework. In the present context this could be the time needed by the basic wave to cover one atmospheric scale height, after which its amplitude would have changed by a factor of $e^{1/2}$, an effect not described within the Boussinesq approximation. Another interesting time scale is the HGW period $P=2\pi/|\Omega|$. Since it is here also not too far from the time needed by the wave to cover one atmospheric scale height, it has instead been chosen as examined long-optimization time.

The SV growth factors for the slightly subcritical IGW ($a=0.87$) are shown in Fig. 9 for $\tau=15$ min, 30 min, 1 h, and 2 h. Three aspects are interesting. Firstly, at longer-optimization times transverse SVs are favored. Secondly, optimal growth is strongest around $\tau=30$ min, with a value

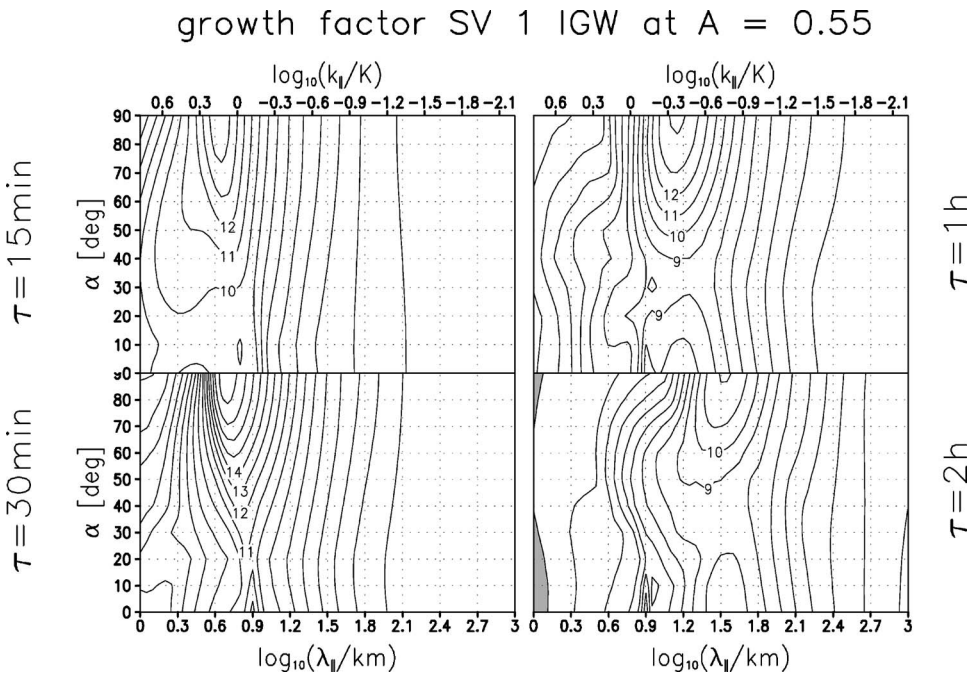

FIG. 9. As a function of parallel wavelength $\lambda_\parallel$ (or wavenumber $k_\parallel$, top axis) and azimuthal angle α, the growth factors of the leading SV of the slightly subcritical IGW [$\Theta=89.5°$ and $(a,A)=(0.87,0.55)$], for the optimization times $\tau=15$ min, 30 min, 1 h, and 2 h. The contour interval is 1, and values less than 1, i.e., the regions without SV growth, are indicated by shading.

Downloaded 03 Nov 2005 to 195.37.145.100. Redistribution subject to AIP license or copyright, see http://pof.aip.org/pof/copyright.jsp

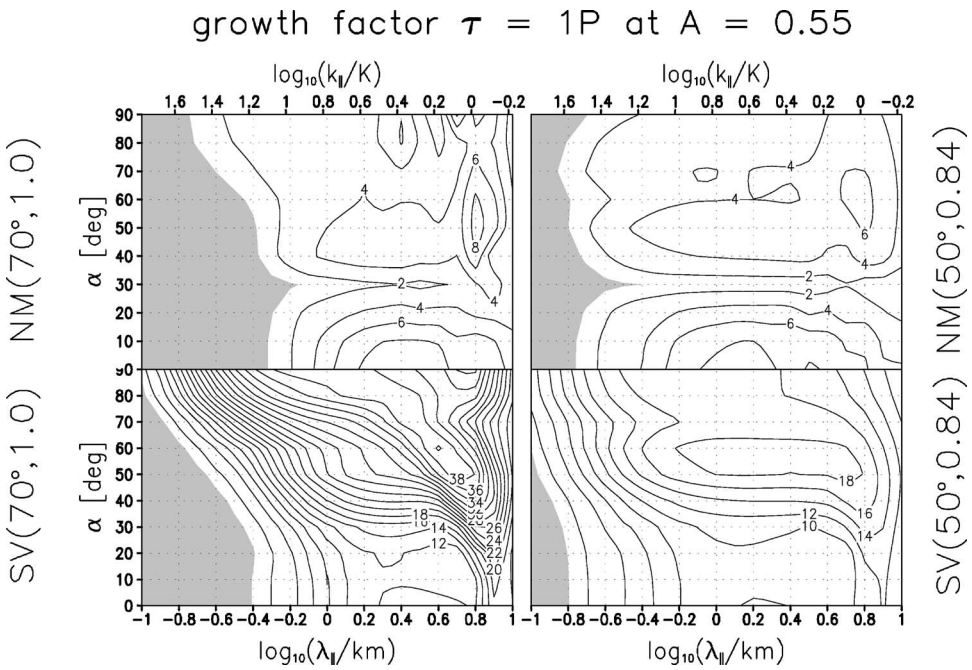

FIG. 10. For $A=0.55$ and as a function of parallel wavelength $\lambda_\parallel$ (or wavenumber $k_\parallel$, top axis) and azimuthal angle α, the growth factors of leading NM (top row) and leading SV (bottom) for growth over one wave period $\tau=P$, for the HGW cases $\Theta=70°$ (left column, $P=920$ s) and $\Theta=50°$ (right, $P=490$ s). The contour interval is 2, and values less than 1, i.e., the regions without NM or SV growth, are indicated by shading.

near 20. Thirdly, the dominant scales generally increase with τ. For the IGW packet case the increase in the growth factors for longer τ (here between 5 and 30 min), as well as the increase in horizontal wavelength and the tendency of transverse perturbations to grow most rapidly at larger τ, is analyzed in detail in AS12. Under the assumption that only the local conditions near the statically least stable location $\phi=3\pi/2$ enter, it is found that the mechanism responsible for optimal growth at $\alpha=0$ allows a maximal growth, approached for large τ, of $\sigma_1^2=4/\mathrm{Ri}_l N^2/N_{\mathrm{tot}}^2$, where $\mathrm{Ri}_l=N_{\mathrm{tot}}^2/\beta^2$ is the local Richardson number, determined by the local vertical gradient of the transverse velocity in the IGW $\beta=af\tan\Theta$ and the local total squared Brunt-Vaisala frequency $N_{\mathrm{tot}}^2=(1-a)N^2$. At fixed vertical scale the horizontal scale is $\lambda_\parallel\propto\tau$. Transverse perturbations, on the other hand, are amplified by a mechanism which allows optimal growth to increase without bounds over a wider span of τ (before viscous-diffusive effects become important). For these one has the rough identity $\tau=m_0/(\beta k_\parallel)$, where m_0 is an initial typical vertical scale of the perturbation. Indeed it is found that, e.g., the structure of the leading transverse optimal perturbation for $\tau=15$ min is that of a wave packet near the statically least stable location with vertical scale about twice that of the corresponding structure for $\tau=30$ min (not shown), which fits well since the horizontal scale of both optimal perturbations is about the same. The present calculations thus seem to reproduce the behavior described in AS12. There also a local optimum in SV growth near the same nondimensional τN has been found as here, however, with the modification that at very long τ of the order of the IGW period optimal growth seems to rise again to even larger values (in an approximation of the IGW packet by its vertical profile at the initially statically least stable horizontal location). Corresponding calculations (not shown) indicate no such effect for the monochromatic IGW. An analysis of this discrepancy is beyond the scope of the present study, but the reason could be either in the slightly different wave parameters, the packet envelope, or the one-dimensional (1D) approximation used in AS12 for the longest τ.

Figure 10 shows for the two HGWs at $\Theta=70°$ and $50°$ and $A=0.55$ the SV growth factors, along with those of the NM, for $\tau=P$. As expected, one observes greater similarity between NM and SV growths than at $\tau=300$ s, especially with regard to the $\lambda_\parallel$-α distribution. SV growth maximizes near the locations of the largest NM growth. Thus they also have much larger horizontal scales than the SV at shorter-optimization times. Still, however, one finds about the same ratio between the growth factors as for smaller τ.

B. Energetics and time development

For an analysis of the growth and decay behavior of the respective identified perturbations it seems helpful to resort to energy considerations. For this purpose it is noted that ε satisfies due to (17)–(21)

$$\frac{\partial\varepsilon}{\partial t}+K\frac{\partial}{\partial\phi}\left[-\frac{\Omega}{K}\varepsilon+\Re(\bar{u}_\phi p)-\nu K\frac{\partial}{\partial\phi}\frac{|\mathbf{v}|^2}{2}-\mu K\frac{\partial}{\partial\phi}\frac{|b|^2}{2N^2}\right]=r_u+r_v+r_b+D_v+D_b \tag{28}$$

with

$$r_u=-\Re(\bar{u}_\xi u_\phi)K\frac{dU_\xi}{d\phi}, \tag{29}$$

$$r_v=-\Re(\bar{v}u_\phi)K\frac{dV}{d\phi}, \tag{30}$$

$$r_b=-\Re(\bar{b}u_\phi)\frac{K}{N^2}\frac{dB}{d\phi}, \tag{31}$$

$$D_v=-\nu\left[(\kappa^2+\lambda^2)|\mathbf{v}|^2+K^2\left|\frac{\partial\mathbf{v}}{\partial\phi}\right|^2\right], \tag{32}$$

Downloaded 03 Nov 2005 to 195.37.145.100. Redistribution subject to AIP license or copyright, see http://pof.aip.org/pof/copyright.jsp

$$D_v = -\frac{\mu}{N^2}\left[(\kappa^2+\lambda^2)|b|^2 + K^2\left|\frac{\partial b}{\partial \phi}\right|^2\right]. \tag{33}$$

Integrating (28) over a wave period in ϕ removes, due to the periodic boundary conditions, the phase derivative on the left-hand side so that growth and decay can be attributed to contributions from integrals over the right-hand side terms over the wave phase ϕ. These describe the shear-related energy exchange with the basic wave due to countergradient fluxes of u_ξ and v (r_u and r_v), convective exchange by countergradient buoyancy fluxes (r_b), and viscous and diffusive losses (D_v and D_b). This decomposition can be represented in terms of contributions to the instantaneous amplification rate $\Gamma(t)=1/(2\langle\varepsilon\rangle)d\langle\varepsilon\rangle/dt$, which takes the time-independent value $\Gamma=\gamma_\nu$ for a NM. Here angular brackets denote an average over a wave phase so that actually $\langle\varepsilon\rangle=\|\mathbf{x}\|^2/2\pi$ in the notation used above. Using the instantaneous amplification rate and its decomposition

$$\Gamma = \Gamma_u + \Gamma_v + \Gamma_b + \Gamma_d = \frac{\langle r_u\rangle}{2\langle\varepsilon\rangle} + \frac{\langle r_v\rangle}{2\langle\varepsilon\rangle} + \frac{\langle r_b\rangle}{2\langle\varepsilon\rangle} + \frac{\langle D_v + D_b\rangle}{2\langle\varepsilon\rangle}, \tag{34}$$

the following gives an analysis of the processes responsible for the growth and decay of the leading NM or SV. The focus is on the latter, but a comparative analysis of the corresponding NM seems in place as a reference.

With respect to NM a caveat shall be mentioned concerning a possible misinterpretation of the amplification-rate decomposition. It can happen that one of the amplification-rate contributions introduced above is large and still the corresponding gradient in the basic-wave field does not cause the NM growth behavior. To show this a further coordinate transformation is applied in which the axes in the ξ-y plane are rotated so that the axes for the new coordinates, denoted by $x_\parallel$ and $y_\perp$, point in the direction of the horizontal wavenumber vector of the perturbation and orthogonal to it, i.e., $x_\parallel=\xi\cos\alpha+y\sin\alpha$ and $y_\perp=-\xi\sin\alpha+y\cos\alpha$. The corresponding velocity components of $\mathbf{v}$ and $\mathbf{V}$ are $(u_\parallel, v_\perp)$ and $(U_\parallel, V_\perp)$. With $k_\parallel=\sqrt{\kappa^2+\lambda^2}$ one obtains from (17)–(21)

$$ik_\parallel u_\parallel + K\frac{\partial u_\phi}{\partial\phi} = 0, \tag{35}$$

$$\frac{Du_\parallel}{Dt} + Ku_\phi\frac{dU_\parallel}{d\phi} + ik_\parallel p + b\cos\alpha\cos\Theta + f(\sin\alpha\cos\Theta u_\phi - \sin\Theta v_\perp) = \nu\nabla^2 u_\parallel, \tag{36}$$

$$\frac{Dv_\perp}{Dt} + Ku_\phi\frac{dV_\perp}{d\phi} - b\sin\alpha\cos\Theta + f(\sin\Theta u_\parallel + \cos\alpha\cos\Theta u_\phi) = \nu\nabla^2 v_\perp, \tag{37}$$

$$\frac{Du_\phi}{Dt} + K\frac{\partial p}{\partial\phi} - b\sin\Theta - f\cos\Theta(\sin\alpha u_\parallel + \cos\alpha v_\perp) = \nu\nabla^2 u_\phi, \tag{38}$$

$$\frac{Db}{Dt} + Ku_\phi\frac{dB}{d\phi} + N^2[\sin\Theta u_\phi - \cos\Theta(\cos\alpha u_\parallel - \sin\alpha v_\perp)] = \mu\nabla^2 b, \tag{39}$$

where here $D/Dt=\partial/\partial t-\Omega\partial/\partial\phi+ik_\parallel U_\parallel$. It turns out that $v_\perp$ is coupled to the other variables only passively provided that the Coriolis terms are negligible for the perturbation dynamics, which seems always to be the case here, and $\cos\Theta\sin\alpha\approx 0$. The latter implies either the IGW case or parallel horizontal propagation of the perturbation with respect to the gravity wave. Then $u_\parallel$, u_ϕ, and b can be considered independently from $v_\perp$, and taking all these to be proportional to $\exp(-i\omega_\nu t+\gamma_\nu t)$ the eigenfrequency and growth rate of all NMs can be determined from Eqs. (35), (36), (38), and (39) alone. Thus, in the IGW case they do not depend on $V_\perp$. A contribution of the corresponding shear term to the amplification rate indicates something different. Since in a NM up to the oscillating phase factor all fields grow or decay in strict proportion one also has for IGW ($\cos\Theta\approx 0$), with the obvious transformations $(r_{u,v},\Gamma_{u,v})\to(r_{\parallel,\perp},\Gamma_{\parallel,\perp})$, and neglecting for the moment the generally weak impact from viscosity and diffusion, the identity $\langle r_\parallel+r_w+r_b\rangle/\langle|u_\parallel|^2+|w|^2+|b|^2/N^2\rangle\approx r_\perp/\langle|v_\perp|^2\rangle$ so that

$$\frac{\Gamma_\perp}{\Gamma_\parallel+\Gamma_w+\Gamma_b} \approx \frac{\langle|v_\perp|^2\rangle}{\langle|u_\parallel|^2+|w|^2+|b|^2/N^2\rangle}. \tag{40}$$

Thus a large contribution from $\Gamma_\perp$ tells us that the NM contains a correspondingly large part of its energy in the flow field $v_\perp$ which indeed is extracted from the wave via a momentum flux against the shear in $V_\perp$, but at a rate independent from this gradient.

In the case of SV the interpretation of the amplification-rate decomposition must be somewhat different. In some way it turns out to be less subtle. There the dynamical fields do not grow in strict proportion. A single growth rate, characterizing the identical rate at which energy is transferred from the basic wave into the various perturbative fields, does not exist. On the contrary the energetics of the perturbation is determined by the sum of all the contributions listed above which can be highly time dependent not only in their magnitude but also in their relative importance. This time dependence must be traced in order to comprehend the full dynamics. Still, in the IGW case one finds that $v_\perp$ reacts only passively to changes in the other perturbative fields. In contrast to the NM case, however, a large $\Gamma_\perp$ does not simply tell us that much energy is in $v_\perp$, which yet grows at a rate determined by all fields in the basic wave except $V_\perp$. It rather indicates that the growth or decay of the energy in the SV is to a large part to be attributed to a corresponding growth or decay in the energy in $v_\perp$, which indeed is induced by the gradient in $V_\perp$ and a corresponding momentum flux $\Re(\bar{v}_\perp u_\phi)$ in the perturbation. In fact, widely differing values in the amplification-rate contributions are often a sign of considerably disproportionate amplifications of the energy content in the various dynamical fields.

Downloaded 03 Nov 2005 to 195.37.145.100. Redistribution subject to AIP license or copyright, see http://pof.aip.org/pof/copyright.jsp

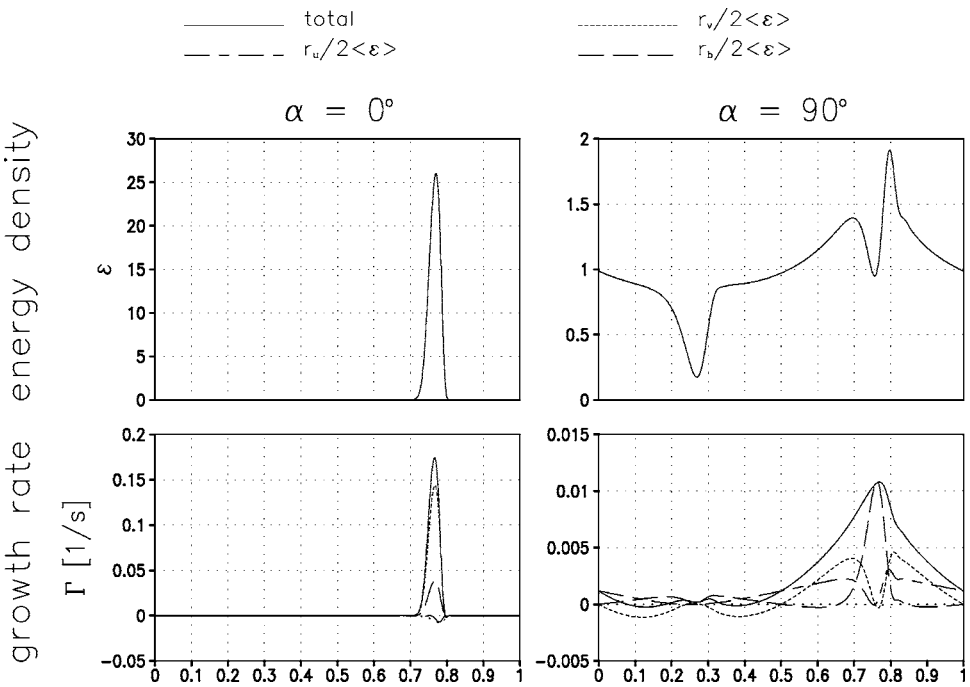

FIG. 11. IGW-phase dependence of energy density (top row) and growth-rate decomposition (bottom) of the leading parallel and transverse NMs for the convectively unstable IGW ($a=1.2$, $\Theta=89.5°$). The IGW-phase average of the sum of all growth-rate parts yields the total growth rate $\Gamma=\gamma_1$. The unimportant contribution from viscous and diffusive losses is indicated by a dotted line. The amplitude of the NM (in meaningless units) has been chosen to normalize the IGW-phase average of energy density ($\langle\varepsilon\rangle=1$).

1. Inertia-gravity waves

In the investigation of the dynamics of the identified perturbations the beginning shall be made by a discussion of those found in the stability analysis of the IGW ($\Theta=89.5°$). Basically most results from AS12 are retrieved, now, however, for monochromatic IGW instead of IGW packets.

a. Short-optimization times. To begin with the case of $\tau=300$ s, Fig. 11 shows for the convectively unstable case ($a=1.2$) the spatial dependence of energy density ε and the IGW-phase-dependent amplification-rate decomposition [i.e., the right-hand side (RHS) terms of (28), normalized by $2\langle\varepsilon\rangle$] of the leading parallel ($\alpha=0°$) and transverse ($\alpha=90°$) NMs. The structures are quite different. The parallel mode is highly concentrated near the region of the strongest convective instability due to the wave-related negative buoyancy gradient. The main contribution to its positive growth rate is apparently from r_v, with another one from r_b. However, since we are looking at the stability problem of an IGW the caveat from above applies. For a parallel NM $U_\parallel=U_\xi$, and thus its growth rate is only determined by the gradients of U_ξ and B. Therefore the convective exchange seems to dominate the dynamics of this mode while much of its energy turns out to be in v. In comparison to this NM, the leading transverse mode is much broader, but it also obtains its energy to an important part via the convective exchange term r_b in the region of the strongest convective instability (near $\phi=3\pi/2$). As is seen in Table II, where the IGW-phase-averaged amplification-rate decomposition is listed, Γ_u makes the largest contribution, but also here in reality Γ_v and Γ_b are the essential terms in determining (to about equal contributions) the growth rate of the NM. The large contribution from Γ_u indicates that much of the energy of the mode is contained in u.

In comparison to NM, the IGW-phase dependence of energy density and amplification-rate decomposition in a SV is time dependent. Figure 12 shows for the optimal perturbation ($t=0$) and the resulting SV at the optimization time ($t=300$ s) these fields for the leading parallel perturbation (α

TABLE II. For $A=0.55$, the growth-rate decomposition of the leading NM for gravity-wave inclination angle Θ, amplitude a, and mode azimuthal angle α at the perturbation wavelength of the strongest NM growth for the IGW ($\Theta=89.5°$) and the strongest SV growth else.

Θ (°)	a	α (°)	Γ_u (10^{-3} s^{-1})	Γ_v (10^{-3} s^{-1})	Γ_b (10^{-3} s^{-1})	Γ_d (10^{-3} s^{-1})
89.5	0.87	0	−0.15	5.4	1.4	−0.31
89.5	0.87	90	1.1	0.76	0.83	−0.01
70	1.0	0	−1.1	0.01	3.1	−0.65
70	1.0	90	1.1	0.0	0.26	−0.17
50	0.84	0	0.7	0.0	3.9	−0.21
50	0.84	90	1.6	0.0	0.33	−0.30
30	0.55	0	1.2	0.0	4.6	−0.11
30	0.55	70	1.4	0.0	1.6	−0.23

Downloaded 03 Nov 2005 to 195.37.145.100. Redistribution subject to AIP license or copyright, see http://pof.aip.org/pof/copyright.jsp

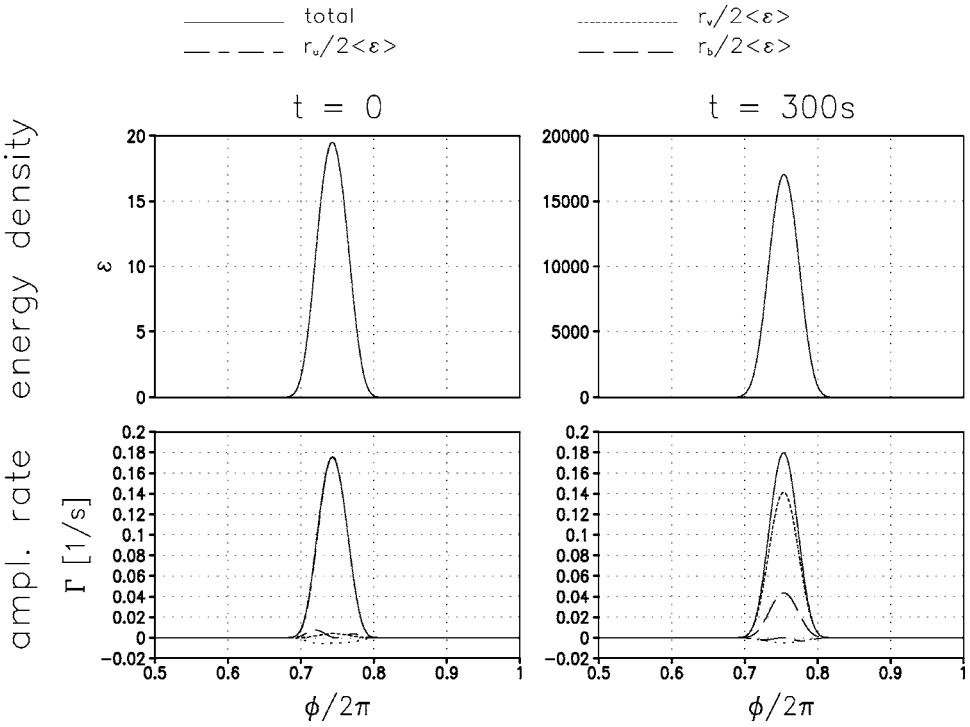

FIG. 12. IGW-phase dependence of energy density (top row) and amplification-rate decomposition (bottom) of the leading parallel singular vector ($\alpha=0$) for the convectively unstable IGW ($a=1.2$, $\Theta=89.5°$) at initialization ($t=0$) and optimization times ($t=300$ s). The IGW-phase average of the sum of all amplification-rate parts yields the total instantaneous amplification rate Γ. The unimportant contribution from viscous and diffusive losses is indicated by a dotted line. The amplitude of the perturbation (in meaningless units) has been chosen to normalize the IGW-phase average of energy density ($\langle\varepsilon\rangle=1$) at $t=0$. Only the IGW-phase range $\pi \leqslant \phi \leqslant 2\pi$ is shown where the SV has a significant amplitude. At $t=0$ the total effective amplification rate is nearly identical with the convective contribution $r_b/2\langle\varepsilon\rangle$.

$=0$). At first sight it looks similar to the leading NM, since it is also highly concentrated in the convectively most unstable phase region. The amplification-rate contributions are, however, quite different. At initialization virtually all of the energy transfer from basic wave to SV is done convectively, while by $t=\tau$ the state of the NM has been approached, where the shear-related exchange r_v is largest, followed by the convective contribution. In Fig. 13 one can see the leading transverse SV ($\alpha=90°$). This perturbation is much more concentrated in the convectively most unstable region than the corresponding NM. Also here the convective energy exchange makes the largest contribution at the initialization, followed by another important one from r_v, while by the optimization time r_u also contributes significantly, and r_v has become rather unimportant. It is to be noted that in this case at the perturbation wavelength where SV growth maximizes no growing NM exists (see Figs. 7 and 8) so that by $t=\tau$ the SV structure cannot be explained in terms of a related NM.

This distinction gets even clearer as one looks at the time-dependent amplification-rate decomposition, according

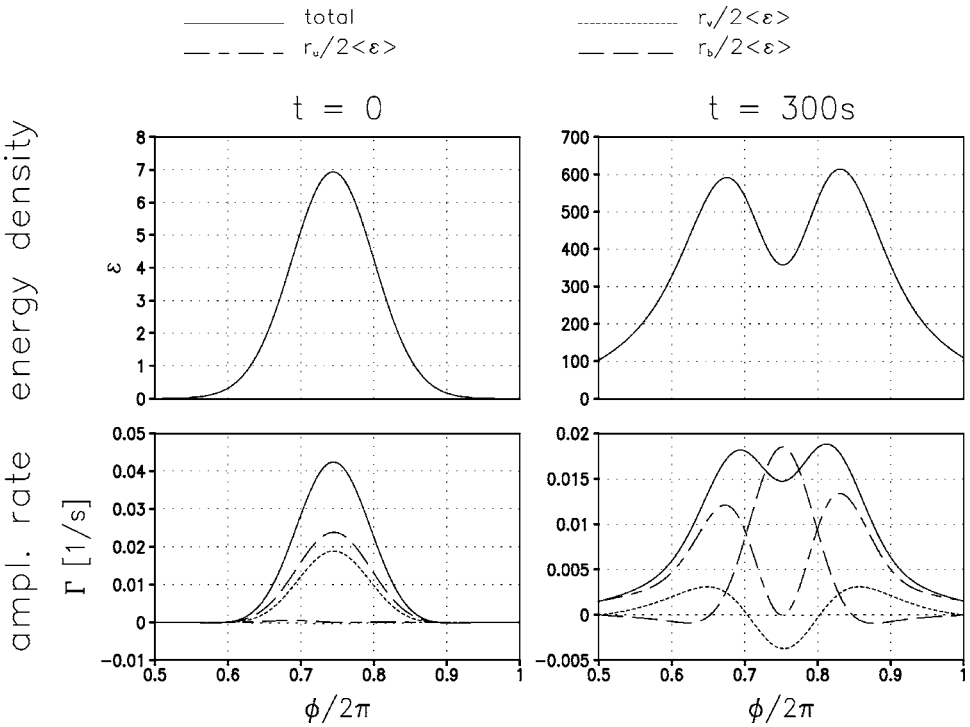

FIG. 13. As Fig. 12, but now for the leading transverse SV ($\alpha=90°$).

Downloaded 03 Nov 2005 to 195.37.145.100. Redistribution subject to AIP license or copyright, see http://pof.aip.org/pof/copyright.jsp

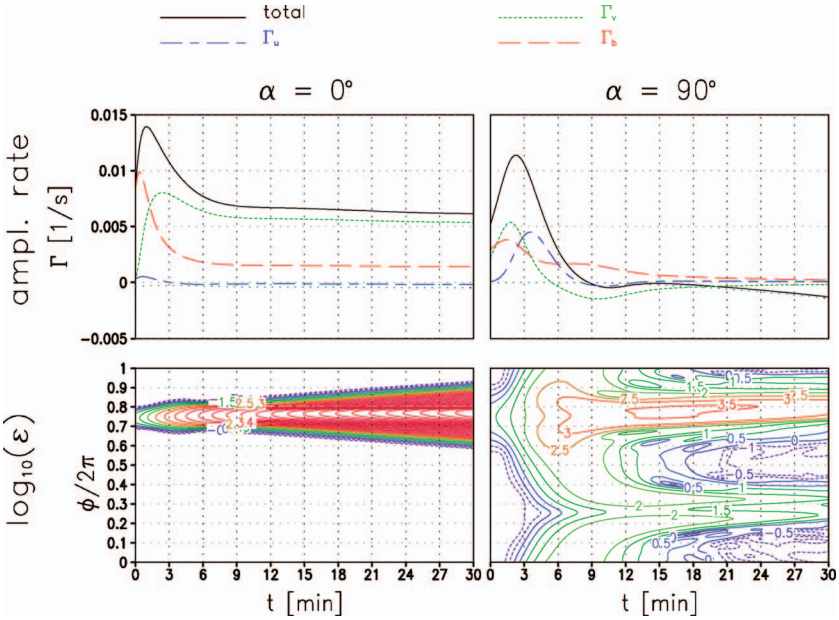

FIG. 14. (Color) Time-dependent amplification-rate decomposition (top row) and energy density (bottom) from 30-min integrations of the leading parallel (left column) and transverse (right) SVs for the convectively unstable IGW ($a=1.2$, $\Theta=89.5°$). The optimization time is $\tau=5$ min. The viscous and diffusive losses are indicated by a dotted line. The contour interval in the lower panels is 0.5 in $\log_{10}(\varepsilon)$ (starting at -1). The negative contours are dashed.

to (34), and energy density ε from somewhat longer integrations. These are shown for an integration over 30 min in Fig. 14. The parallel SV exhibits a time-dependent amplification-rate decomposition with a maximum total value around $t=1$ min, when the initially dominant contribution from convective energy exchange is supplemented by that from the countergradient flux in v. By $t=9$ min a state is reached where the amplification rate does not vary anymore, both in its total value and in its decomposition in the various contributions (a leading contribution from shear in V with an additional weaker term from convective energy exchange). This indicates that the perturbation has assumed the structure of the leading NM and keeps on growing from there on. The energy density supports this picture. One sees a perturbation basically invariant in structure which is simply growing exponentially in time. The leading transverse SV, on the other hand, does not approach such an asymptotic behavior. Its amplification rate maximizes around $t=2$ min then decreases until decay sets in at about $t=9$ min which at late times is dominated by viscous and diffusive losses ($\Gamma \approx \Gamma_d$). But even then the amplification-rate decomposition stays time dependent. The energy density shows that the SV is split up into two main substructures, one of these at the original location of the initial perturbation, i.e., near the strongest convective instability, and the other one near the other zero line of the transverse wind in the IGW ($\phi=\pi/2$). As is shown in AS12 for a similar case the SV radiates gravity waves which are approaching a quasicritical layer near the transverse-wind zero line, where their propagation is blocked and very small scales develop, thus explaining the observed behavior. A short discussion of this effect is given in the Appendix.

At a weaker IGW amplitude ($a=0.87$), where NM can no longer grow, basically the same type of parallel and transverse SVs is found. Their time-dependent behavior is plotted in Fig. 15. Now one sees both eventually decay in time, with a maximum in energy around $t=7$ min. The time-dependent decomposition of the instantaneous amplification rate is very similar to the one seen at the stronger IGW amplitude. In both cases convective instability seems to act as a trigger of the instability, while later shear-related exchange plays an important, if not even dominant, role, as in the parallel SV. Although only nonmodal growth is possible the gain in energy covers several orders of magnitude, indicating that at a suitable initial perturbation level SV might be able to initialize nonlinear behavior and onset of turbulence. An interesting observation also is that in all cases shear in $V_\perp$ plays an important role, indicating that the amplification of the SV is to a large part due to energy growth in $v_\perp$.

b. Long-optimization times. Getting to the case of the longer-optimization times the focus shall be on the global optimal $\tau=30$ min for $a=0.87$. Time-dependent amplification-rate decomposition and energy density of the leading parallel and transverse SVs for $a=0.87$ are shown in Fig. 16. Similar to the results in AS12 the time dependence scales with τ, i.e., energy growth persists until $t=\tau$, after which decay sets in (the same behavior is also seen for all other τ, not shown). Also here convective exchange acts as a trigger, followed by the action of the countergradient fluxes in the horizontal velocity field. In comparison to the short-optimization time, the flux in v takes a less prominent role for the leading parallel SV but a dominant role in the transverse case. The energy density indicates in the latter case similar critical-layer interactions as for $\tau=300$ s. Indeed the time-dependent buoyancy field in Fig. 17 shows this behavior, i.e., a tendency towards increasingly smaller scales near the zero lines of V, a behavior which has been analyzed in depth in AS12 (but see also the Appendix). For the leading parallel SV a quite different behavior can be seen. In contrast to the transverse SV the vertical scales progressively increase near $\phi=\pi/2$. This is different to the behavior seen in AS12, where the wave-packet envelope allowed the outwards radiation of high-frequency gravity waves. Here one sees a dynamics modified essentially by the periodic flow field in the basic IGW, leading to a ducting effect, where the SV, oscillating at a frequency $\omega=\kappa U_\xi(\phi=3\pi/2)$, is prevented from

Downloaded 03 Nov 2005 to 195.37.145.100. Redistribution subject to AIP license or copyright, see http://pof.aip.org/pof/copyright.jsp

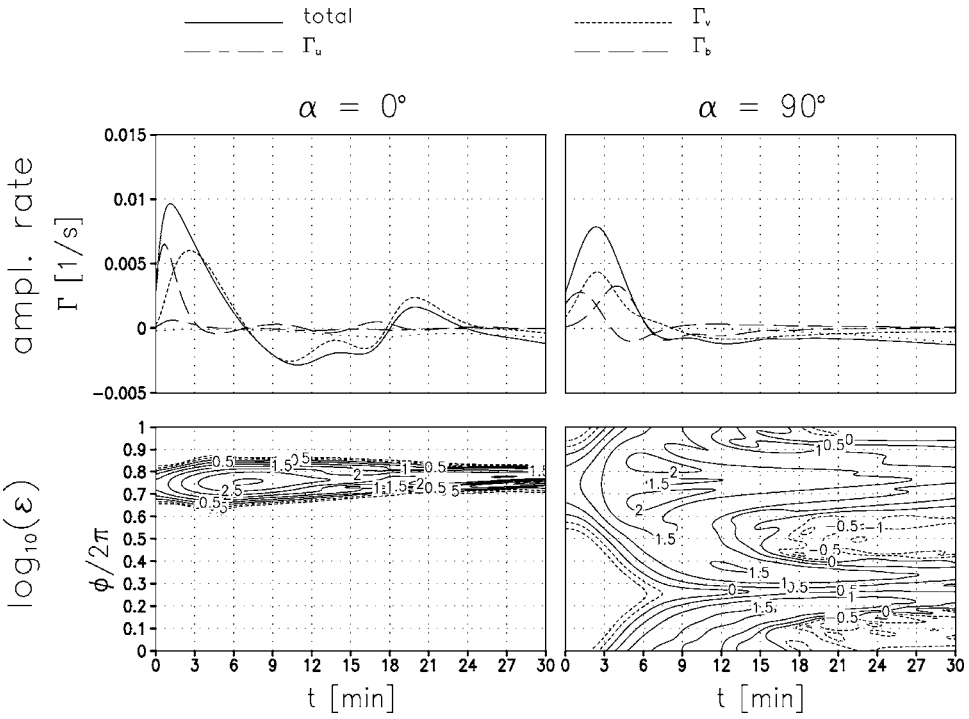

FIG. 15. As Fig. 14, but now for an IGW amplitude $a=0.87$ excluding the possibility of NM instabilities.

radiating through the maximum of U_ξ. Details are given in the Appendix.

A comparison of the relevance of the SV for short- and long-optimization times, although desirable, must remain incomplete on the level of the present linear analysis. Note that, although showing larger overall growth, the long-optimization-time SVs grow at a smaller growth rate than the SVs for shorter τ. This makes cases conceivable where, at sufficiently large initial perturbation level, the latter SVs lead the IGW into nonlinear behavior, before the ones for longer τ have fully developed. A case of weaker initial perturbations where the stronger overall growth of the slower developing SV is necessary for an initialization of the nonlinear development might, however, also be thought about. More conclusive answers to such questions must wait for a nonlinear treatment of this transition problem.

2. High-frequency gravity waves

In contrast to the two subcritical IGW cases examined here, i.e., with $a<1$ and $\mathrm{Ri}>0.25$ (see Table I), HGWs show NM activity at virtually all amplitudes. Thus after nearly

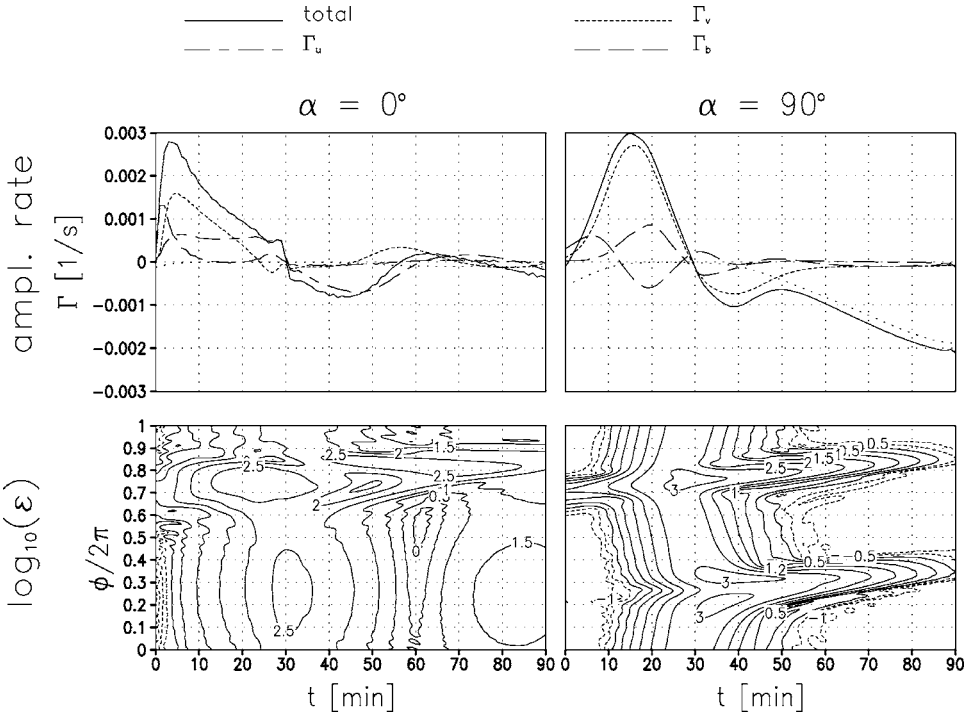

FIG. 16. As Fig. 14, but now for an IGW amplitude $a=0.87$ excluding the possibility of NM instabilities (as in Fig. 15) and optimization time $\tau=30$ min.

Downloaded 03 Nov 2005 to 195.37.145.100. Redistribution subject to AIP license or copyright, see http://pof.aip.org/pof/copyright.jsp

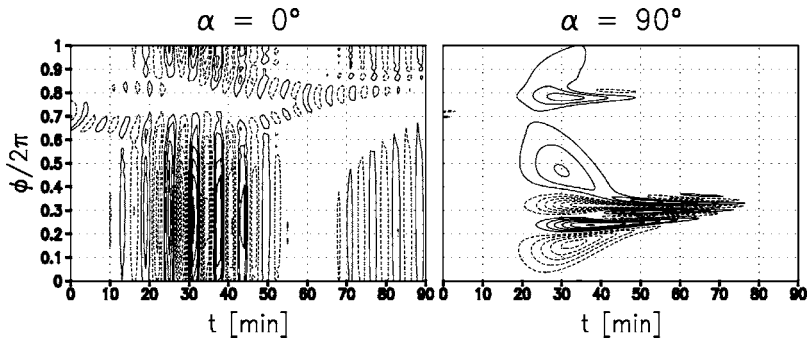

FIG. 17. Corresponding to Fig. 16, the development of the buoyancy field in the respective SVs. The contour intervals are constant in arbitrary units. The zero contour has not been drawn.

every initialization of the linear model eventually the set of the most unstable NM will emerge as the final asymptotic state. The question only is how long it takes until this state is reached. As will be seen below, this time can be quite long, so that under realistic circumstances optimal growth can be of relevance even for these waves.

a. Short-optimization times. The focus shall first be on the short-optimization time $\tau=300$ s. At least qualitatively the different HGW cases turn out to be very similar in the comparative dynamics of NM and SV. As an example here the case $\Theta=70°$ and $a=1$ (i.e., $A=0.55$) is discussed in some detail. Figure 18 shows for these parameters the HGW-phase dependence of energy density and amplification-rate decomposition for the leading parallel and transverse NMs, each for the wavelength at which optimal growth maximizes (see Fig. 6). In addition, Table II also lists the HGW-phase integral of the growth-rate decomposition. The results agree with those from Lombard and Riley[27] in that the parallel mode is mainly excited convectively, while the transverse mode extracts its energy from the gravity wave predominantly via shear-related exchange. Only $dU_\xi/d\phi$ enters the latter since the gravity-wave amplitude in V is negligible. The HGW-phase dependence of the leading exchange terms is consistent with the wave structure. For the parallel mode convective exchange is strongest near $\phi=3\pi/2$, where $dB/d\phi$ is most negative, and the shear exchange for the transverse mode peaks near $\phi=2\pi$ where the wave shear reaches one of its two extrema. As for the complementary exchange terms, one sees wave shear near $\phi=2\pi$ to act against the growth of the parallel mode, while the transverse mode experiences convective excitation at $\phi=\pi/2$, where $dB/d\phi$ becomes largest, an effect which is, however, quite eliminated by strong negative contributions near the flanks of this region so that there is no essential net convective impact on the transverse mode. The respective dominance of the different exchange terms is also reflected in the HGW-phase distribution of the energy density of the NM. The parallel NM is concentrated near $\phi=3\pi/2$, where the convective exchange is largest, and the transverse mode peaks in energy density near $\phi=2\pi$ where the shear-related exchange also maximizes.

Time dependence of amplification-rate decomposition, according to (34), and energy density ε is shown for 30-min integrations of the corresponding SV in Fig. 19. If a single leading NM exists, the final asymptotic behavior can

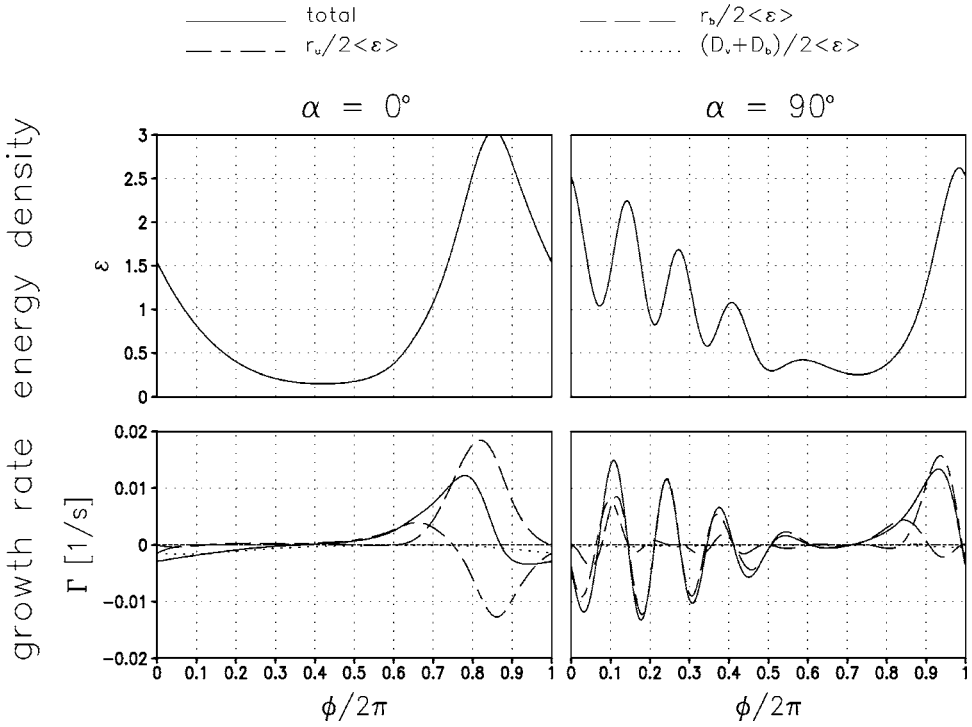

FIG. 18. HGW-phase dependence of energy density (top row) and growth-rate decomposition (bottom) of the leading parallel (left column) and transverse (right) NMs for the high-frequency gravity wave (HGW) with $(\Theta,a)=(70°,1)$, at the perturbation wavelength where optimal growth over 300 s maximizes. The HGW-phase average of the sum of all growth-rate parts yields the total growth rate $\Gamma=\gamma_1$. The negligible contribution to the growth rate from shear in the transverse wind of the wave is indicated by a short-dashed line. The amplitude of the NM (in meaningless units) has been chosen to normalize the HGW-phase average of energy density, i.e., $\langle\varepsilon\rangle=1$.

Downloaded 03 Nov 2005 to 195.37.145.100. Redistribution subject to AIP license or copyright, see http://pof.aip.org/pof/copyright.jsp

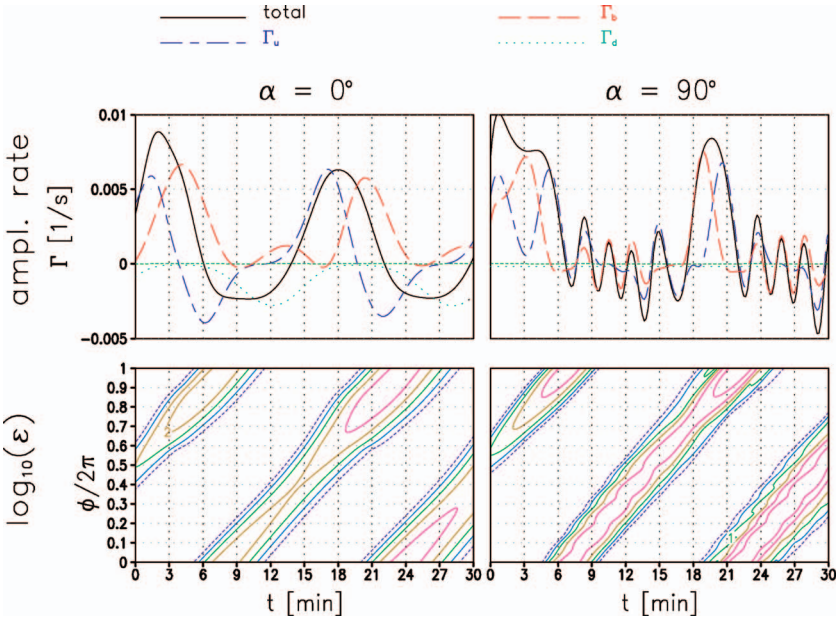

FIG. 19. (Color) Time dependence of the amplification-rate decomposition (top row) and energy density (bottom) from 30-min integrations of the leading parallel ($\alpha=0°$) and transverse ($\alpha=90°$) SVs for a HGW with $(\Theta,a)=(70°,1)$. The initial amplitudes in the patterns (in meaningless units) have been chosen to normalize the HGW-phase average of energy density, i.e., $\langle\varepsilon\rangle=1$. Contouring starts at $\log_{10}(\varepsilon)=-1$. The contour interval is 1. The negative contours are dashed.

be expected as a time-independent amplification-rate decomposition identical to that of that NM (Table II) and an energy density growing in time but not moving with respect to the wave. One notes a slow approach towards this state in two regards. The amplification-rate contributions oscillate with slowly decaying amplitude about the NM values (see Table II), and the energy densities of the two SVs, which indicate highly peaked pulses propagating upwards through the wave, are slowly broadening. As expected from the growth factors, the transverse SV shows more intensive growth than the parallel SV (note the logarithmic color and contour scale). The corresponding behavior after a long time (160 h) is shown in Fig. 20. Indeed the parallel SV has approached the structure of the leading NM, while the transverse SV has split up in finer pulses still moving through the wave, however, with an amplification-rate decomposition seemingly oscillating about the corresponding values of the leading NM. The difference between the two cases arises from the fact that for $\alpha=0°$ a single leading NM exists, while for $\alpha=90°$ two leading NMs are found which are very close to each other in growth rate $[\exp(\gamma_1\tau)=1.4494$ and $\exp(\gamma_2\tau)=1.4491]$ and in their growth-rate decomposition (not shown). Seemingly those two together constitute the basis of the late stage of the development of the corresponding SV. In any case it seems interesting that the eventual approach of the leading NM is rather slow (e.g., by $t=8$ h the NM state has by far not been reached yet, see Fig. 21) so that the transition from SV to NM might take longer than one can expect the linear approximation to hold before nonlinear effects become important. Another main feature one also notes is that the time both SVs need for once covering the distance $\Delta\phi=2\pi$ agrees with the period of the gravity wave (920 s), which means

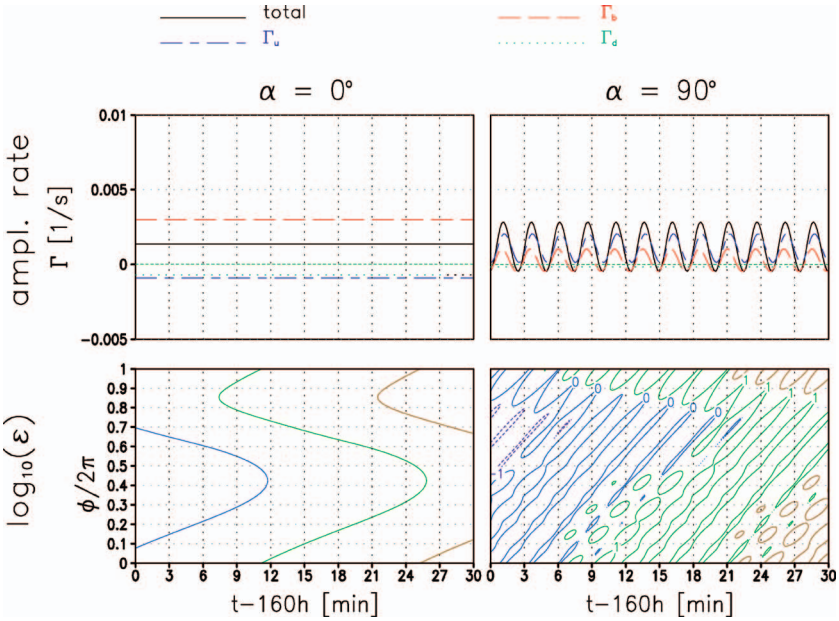

FIG. 20. (Color) As Fig. 19, but for a later phase 160 h$\leq t\leq$160.5 h. ε has been normalized so that its phase average $\langle\varepsilon\rangle=1$ at $t=160$ h.

Downloaded 03 Nov 2005 to 195.37.145.100. Redistribution subject to AIP license or copyright, see http://pof.aip.org/pof/copyright.jsp

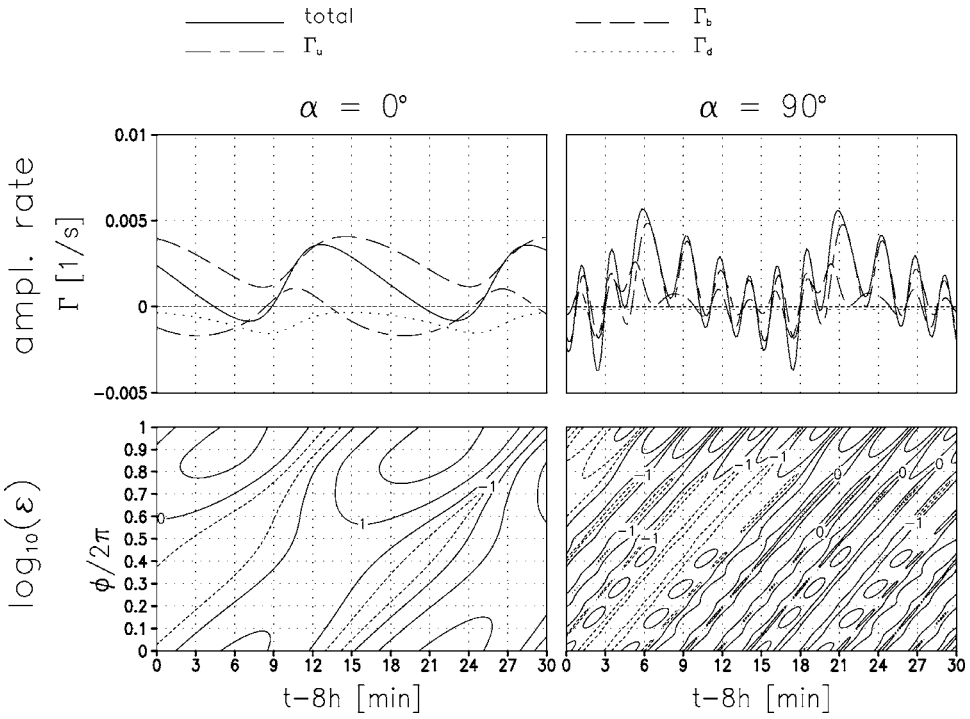

FIG. 21. As Fig. 19, but for a later phase 8 h$\leqslant t \leqslant$8.5 h. ε has been normalized so that its phase average $\langle\varepsilon\rangle$ =1 at t=8 h.

that the perturbation actually does not move in the original reference system while the gravity wave passes over it, at the same time repeatedly invigorating and damping the SV. In the case of a transition to the leading NM one would see the wave gradually picking up the slowly broadening perturbation until its energy-density distribution no longer moves in the translated coordinate system and is basically swept along with the wave as observable for the parallel SV.

Besides this general observation the details of the two time series are also interesting, especially as they reveal impacts from the structures of both the NM and the basic wave. Although the parallel NM grows due to convective exchange the corresponding optimal perturbation is triggered by shear-related exchange. Initially $\Gamma \approx \Gamma_u$ which is consistent with the perturbation being concentrated at $\phi=\pi$ where the wave shear maximizes. By $t \approx 4$ min convective exchange takes over, which is the time when the SV passes the convectively most unstable HGW-phase $\phi=3\pi/2$. Shortly later, when $\phi=2\pi$ is reached, where $dU_\xi/d\phi$ is largest, shear-related exchange is strong again, now, however, damping the perturbation. As the perturbation passes $\phi=\pi/2$ strong viscous and diffusive damping sets in. This is due to a scale contraction of the SV which for one subcycle in the movement between $\phi=0$ and $\phi=2\pi$ is shown in Fig. 22. This behavior can be explained in terms of a WKB-type propagation of the perturbation in the flow field of the gravity wave (see Appendix 3).

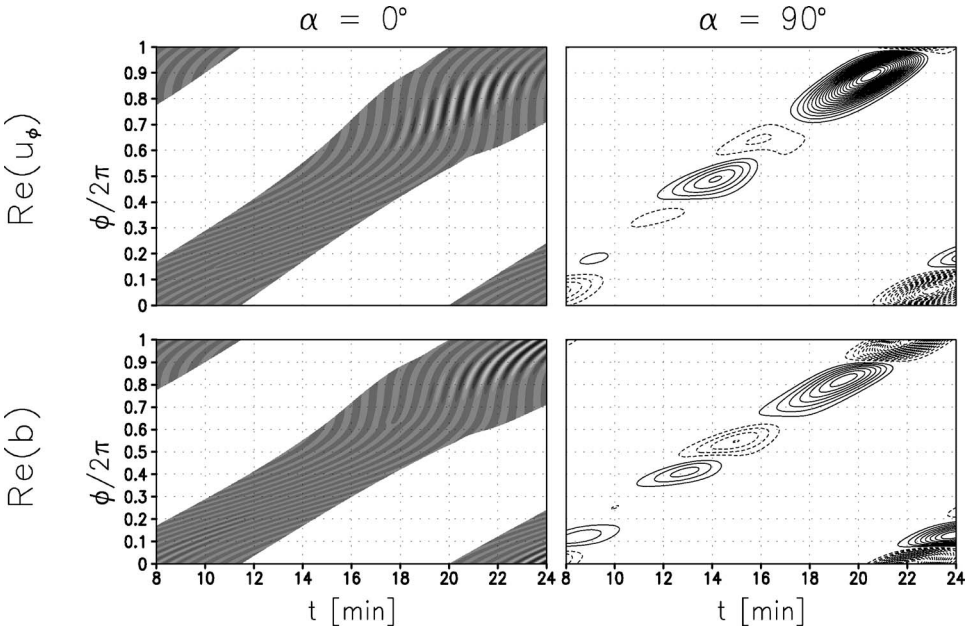

FIG. 22. As Fig. 19, but now showing for one subcycle, corresponding to one passage of the gravity wave over the perturbation, the time-dependent structure of the real parts of u_ϕ (upper row) and b (bottom). Both the shading scale for the parallel perturbation and the contour intervals for the transverse perturbation are linear in arbitrary units. In the latter case the zero contour has not been drawn, and the negative values are indicated by a dashed contour.

Downloaded 03 Nov 2005 to 195.37.145.100. Redistribution subject to AIP license or copyright, see http://pof.aip.org/pof/copyright.jsp

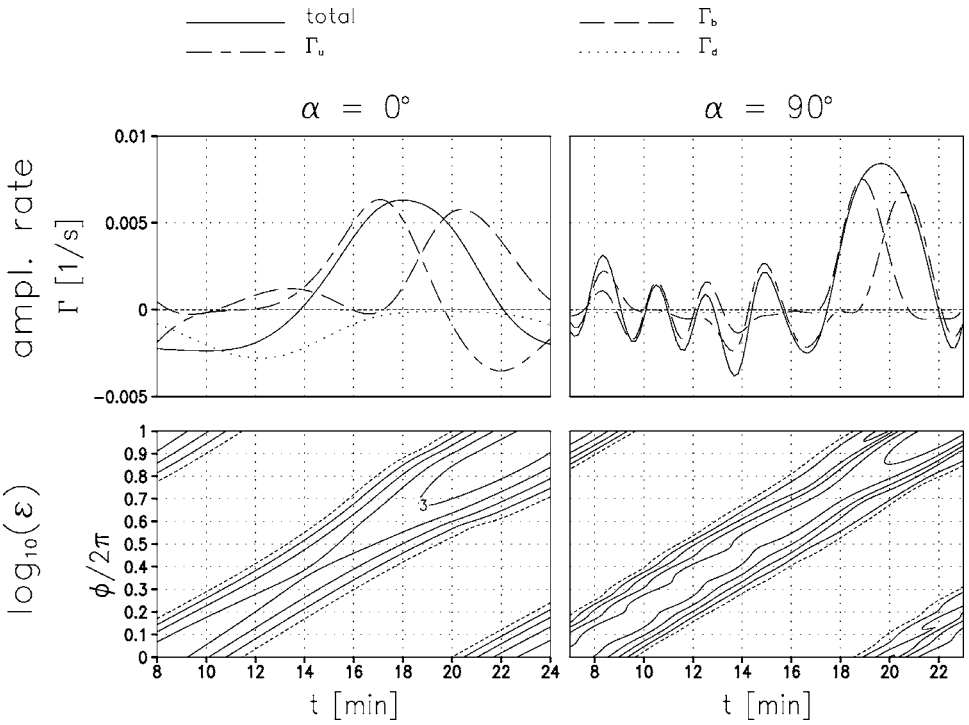

FIG. 23. As Fig. 19, but now for one subcycle corresponding to one passage of the gravity wave over the perturbation.

The succession of processes sketched above is repeated many times as the wave repeatedly passes over the perturbation (not shown). An interesting feature also becomes visible in a comparison of the time-dependent amplification rate of the parallel SV (Fig. 19) with the HGW-phase-dependent analog in the parallel NM (Fig. 18). It appears that in its moving from $\phi=0$ to $\phi=2\pi$ the SV experiences the same exchange processes as the NM exhibits at the respective HGW phase. This goes as far as even expressing itself in the HGW-phase-dependent energy density, i.e., the NM peaks at $\phi=3\pi/2$ while the SV also shows a local maximum in energy density as it passes this HGW phase.

Very similar observations can also be made for the transverse perturbations ($\alpha=90°$, right columns in Figs. 18–22). Also the transverse SV is triggered by shear instability at $\phi=\pi$. As it passes $\phi=3\pi/2$ convective exchange takes over, followed by another peak of Γ_u as $\phi=2\pi$ is reached. This double peak in Γ_u, responsible for the stronger overall growth of the transverse SV in the first 300 s than that of the parallel SV, occurs only once. In the following cycles it is not repeated. Then growth due to shear is only observed at $\phi=2\pi$, preceded by convective growth at $\phi=3\pi/2$, just as observed in the NM. One conspicuous difference between parallel and transverse SVs is that, while the former is a rather small-scale wave packet in its dependence on ϕ, the latter is a larger-scale pulse changing its sign several times in its apparent movement through the HGW. This is the reason (see Fig. 22) why viscosity and diffusion are of less importance for the transverse SV than for the parallel SV. Besides this, as the transverse SV moves from $\phi=0$ to $\phi=3\pi/2$ the instantaneous amplification rate undergoes rapid oscillations which are once again a good copy of corresponding behavior in the NM, as is also the phase distribution of the energy density. In order to facilitate a better comparison a cycle between $\phi=0$ and $\phi=2\pi$ has been redrawn for each SV in Fig. 23.

b. Longer-optimization times. As seen above, the parallel wavelength $\lambda_\parallel$ of the SV for longer-optimization times ($\tau=P$) is larger than for $\tau=300$ s, and their growth-factor distribution in the $\lambda_\parallel$-α plane is more similar to that of the corresponding NM. Interestingly, however, it turns out that their dynamics is still quite similar to that of the SV for $\tau=300$ s. Being once again, at least qualitatively, representative for all cases, here the SVs for the HGW with $(\Theta,a)=(70°,1)$ are discussed shortly. Figure 24 shows the time-dependent amplification-rate decomposition and energy-density distribution for the leading SV at azimuthal angles of 0°, 60° (the case of the strongest optimal growth), and 90°. The similarity of the behavior of the leading parallel and transverse SVs to that seen in Fig. 19 is obvious. As a major difference, in comparison to there the initial amplification rates are smaller, so that initial growth is not as rapid. Also the patterns are broader in structure and thus nearer to the structure of the corresponding NM. Remarkably, however, also here the transition to the NM is far from complete after 30 min, which is nearly two basic-wave periods.

As discussed in the comparison between short- and long-optimization-time SVs for IGW, also for HGW the respective relevance of the corresponding SV can be expected to depend on the properties of the available perturbation spectrum. Mainly its overall intensity will probably be of importance, but also the scales available in it, since the various SVs differ not only in optimization time but also in their intrinsic wavelengths.

Downloaded 03 Nov 2005 to 195.37.145.100. Redistribution subject to AIP license or copyright, see http://pof.aip.org/pof/copyright.jsp

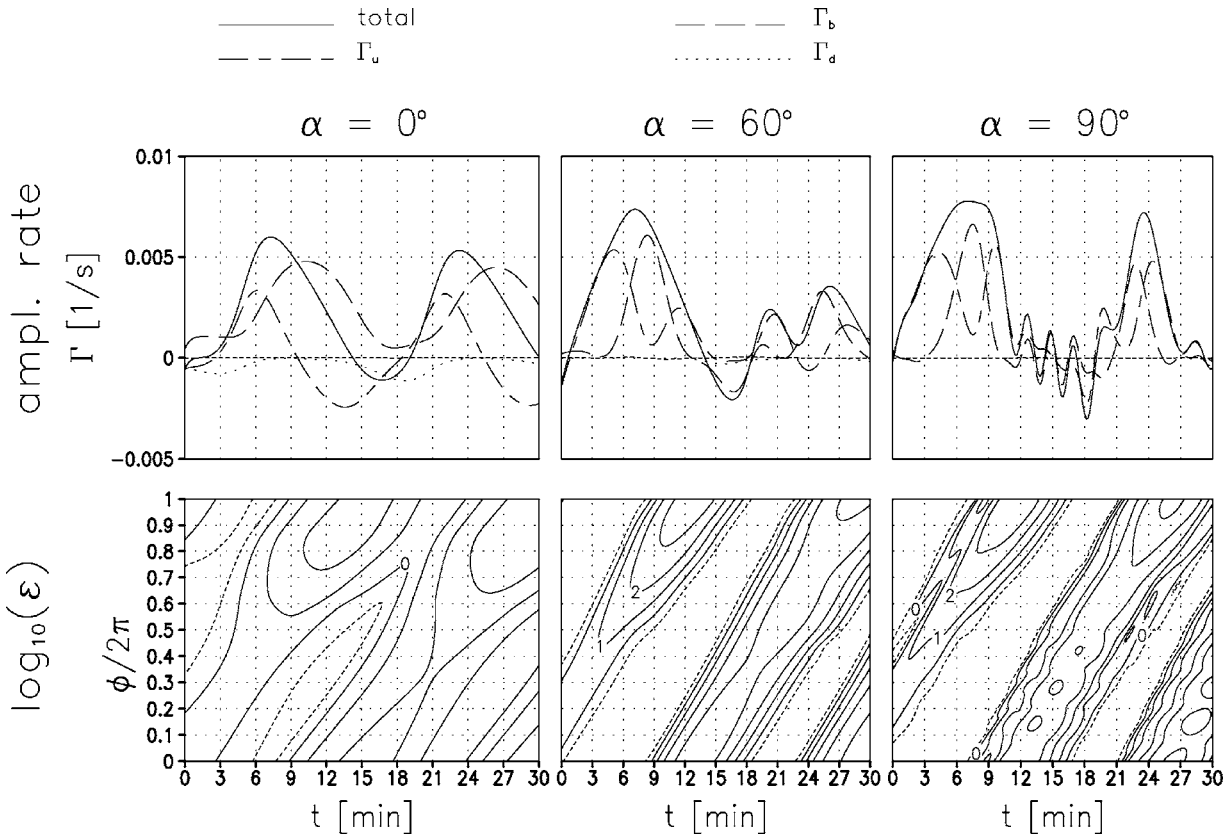

FIG. 24. As Fig. 19, but now for the leading SV for $\tau=P=920$ s and azimuthal angles $\alpha=0°$, 60°, and 90°.

V. IMPACT OF THE CONTROLLING EXTERNAL PARAMETERS

For a complete picture one also needs an overview of what happens as the chosen external model parameters are varied. In the atmosphere, e.g., the inverse proportionality of kinematic viscosity and diffusivity with the background density implies that at fixed wavelength of the gravity wave the Reynolds number decreases from the surface of the earth to the mesopause (at about 90-km altitude) by nearly six orders of magnitude. Likewise varying at fixed altitude the basic-wave wavelength would also imply a variation of the Reynolds number. Another external parameter deserving some examination is the factor f/N. While here f has been chosen to be the Coriolis parameter at 70°N and $N=2\times10^{-2}$ s^{-1}, which is typical for the middle atmosphere, in the tropics, where $f\approx0$, or in the lower atmosphere, where $N=1\times10^{-2}$ s^{-1} is more appropriate a choice, a different dynamics might occur. Without going into too great depth corresponding effects shall be estimated here.

In varying the Reynolds number the above-mentioned six orders of magnitude are not covered. Instead, for reasons of computational economy, viscosity and diffusion have been increased to $\nu=\mu=5$ m^2/s or decreased to $\nu=\mu=0.1$ m^2/s (corresponding to a mid-mesospheric altitude near 70 km), and then the optimal growth over $\tau=300$ s has been determined for $A=0.55$. Figures 25 and 26 show the results. The main effect is as expected. Larger Reynolds numbers mean stronger instabilities. Concerning the $(\lambda_\parallel,\alpha)$ dependence one finds that there is not much of an effect on the azimuthal angles where optimal growth is most vigorous. However, in agreement with similar findings by Lombard and Riley[27] on the dependence of the leading NM for $f=0$ on the Reynolds number, the scales are affected so that the wavelength of the strongest optimal growth gets smaller as the Reynolds number is increased (for IGW AS12 suggest a dependence as $\lambda_\parallel\propto\mathrm{Re}^{-1/4}$, consistent with the results here). An exception to this is the leading transverse SV of the IGW. For this one both the growth factor and its wavelength are found to be basically the same for all three Reynolds numbers examined. This is consistent with the identification of a comparable NM growth-rate peak for $a>1$ by others[31,32] in the calculations for IGW packets with infinite Reynolds number. The main effect here is that, as is visible from a cut at $\alpha=90°$ which is not shown here, while the Reynolds number is increased slowly, a secondary growth-factor peak at a shorter wavelength emerges which is at $\lambda_\parallel\approx600$ m for $\nu=\mu=0.1$ m^2/s. One might expect that this one gets stronger and moves to smaller scales as the Reynolds number is increased even further, while the one at the larger wavelength stays unaffected. Decreasing the Reynolds number would at some stage, however, also damp the growth of that branch. Similarly one also finds for $\Theta=30°$ at $\lambda_\parallel\approx\Lambda$ a parallel SV which is not much affected by viscosity and diffusion, but also here at even smaller Reynolds numbers the SV will probably be damped. For the high-Reynolds-number case NM growth factors (not shown) are found to slightly increase in comparison to Fig. 5 (maximal growth factors of 2.2, 4.0, and 5.8 at $\Theta=70°$, 50° and 30°, with an overall $\lambda_\parallel$-α dependence as before). This

Downloaded 03 Nov 2005 to 195.37.145.100. Redistribution subject to AIP license or copyright, see http://pof.aip.org/pof/copyright.jsp

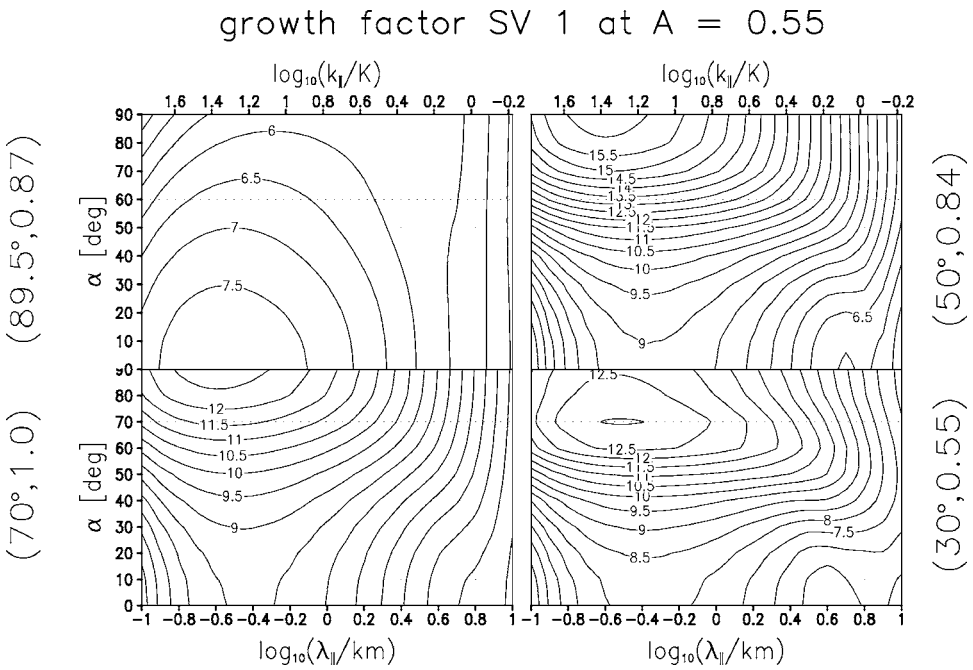

FIG. 25. As Fig. 6, but now with decreased values of viscosity and diffusivity $\nu=\mu=0.1\ \mathrm{m}^2/\mathrm{s}$.

case, however, still shows no NM instabilities of the IGW.

For an estimation of the impact of variations in f/N the determination of the SVs for $A=0.55$ has been redone for different latitudes. As expected only the IGW case showed an impact so that only this one shall be given some attention. Figure 27 shows the $(\lambda_\parallel, \alpha)$ dependence of the growth factors of the leading SV obtained for the latitudes of 0°, 30°, 50°, and 90°, to be compared to the upper left panel in Fig. 6. One sees two main effects: As rotation becomes smaller optimal growth gets weaker and the leading azimuthal angle moves from parallel to $\alpha=60°$. The former is consistent with the previous observation that the energy exchange with the IGW via shear in V plays an important role. As rotation gets less the strength of this wind component in the wave is reduced so that the energy reservoir of its kinetic energy provides for the SV is reduced. In time integrations (not shown) the SVs are found to finally decay in all cases, as also follows from the absence of growing NM. It seems that optimal growth is not so important for subcritical IGW in the tropics.

VI. MEAN GROWTH FROM RANDOM INITIAL CONDITIONS

A critical question one might ask about rapid transient growth from optimal perturbations is how relevant they are for realistic circumstances where a gravity wave will encounter perturbations from ambient fluctuations which most probably will not project to the largest part onto a single optimal

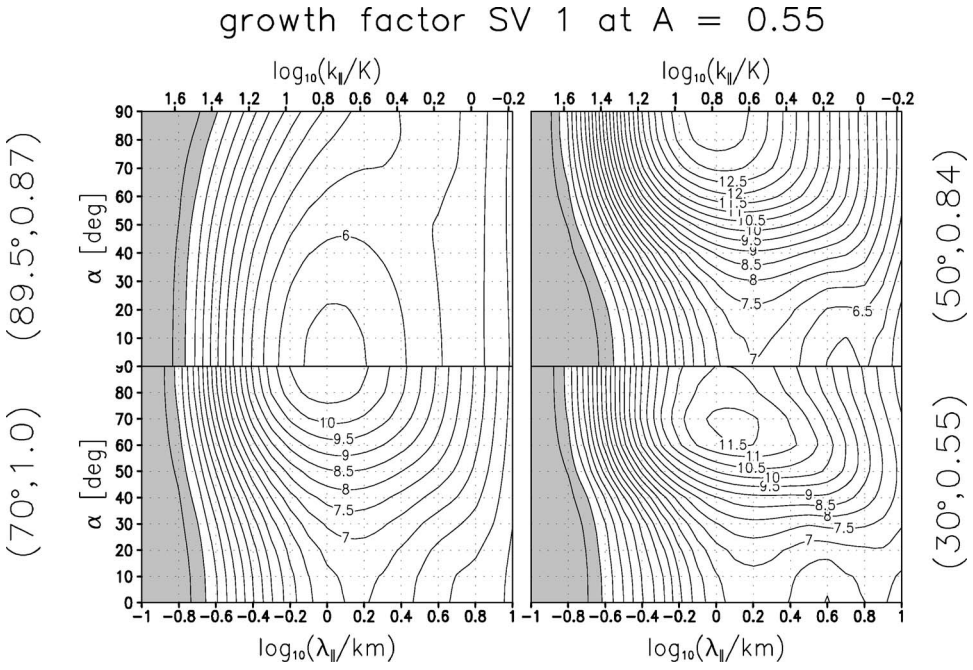

FIG. 26. As Fig. 6, but now with increased values of viscosity and diffusivity $\nu=\mu=5\ \mathrm{m}^2/\mathrm{s}$.

Downloaded 03 Nov 2005 to 195.37.145.100. Redistribution subject to AIP license or copyright, see http://pof.aip.org/pof/copyright.jsp

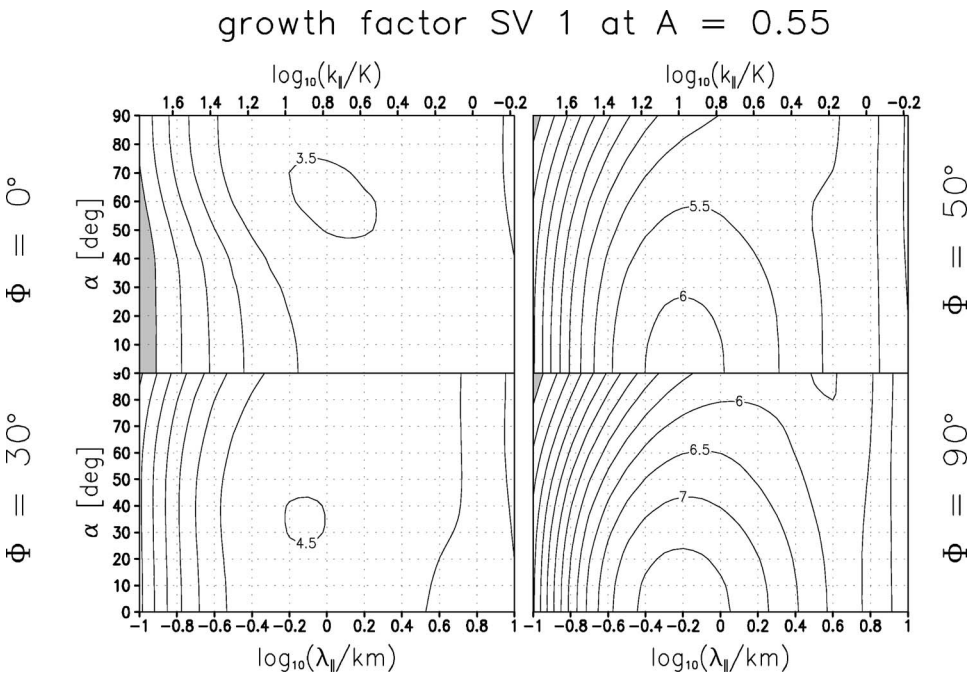

FIG. 27. $(\lambda_{\|},\alpha)$ dependence of the growth factors of the leading SV for a slightly subcritical "IGW" $[(\Theta,a)=(89.5°,0.87)]$ at the latitudes $\Phi=0°$, 30°, 50°, and 90°, determining the magnitude of the Coriolis parameter. The contour interval is 0.5. Values less than 1 are indicated by shading.

perturbation.[47] If there is only one SV structure having rapid growth, it may not be sufficient to compete with the leading normal mode (if there is any). If, however, the number of growing optimal perturbations is large enough, and if these are similar enough to each other, optimal growth might play a role in explaining the observed behavior of turbulence onset in its linear phase.

In order to get some insight into this problem the linear model has been integrated over 300 s from random initial conditions. A possible option for a source spectrum would be just white noise, but this would not be overly realistic. Rather it is to be expected that a gravity wave will encounter fluctuations with a typical turbulent spectrum, as observed[7] and modeled[19,20] by others. It has therefore been attempted to mimic a spectrum in the wavenumber in ϕ direction with a typical 5/3 power law. For this energetically equipartitioned flow and buoyancy fields have been obtained from a random number generator. The Fourier transforms of these have then been modified to follow a 5/3 power law, and the resulting random initial states have then been used in the model. For each pair of azimuthal angle and perturbation wavelength in the ξ-y plane the number of integrations has been doubled, starting at a minimum of 16, until the observed mean growth or decay in the square root of energy changed by less than a percent.

For $A=0.55$ the resulting mean growth is shown in Fig.

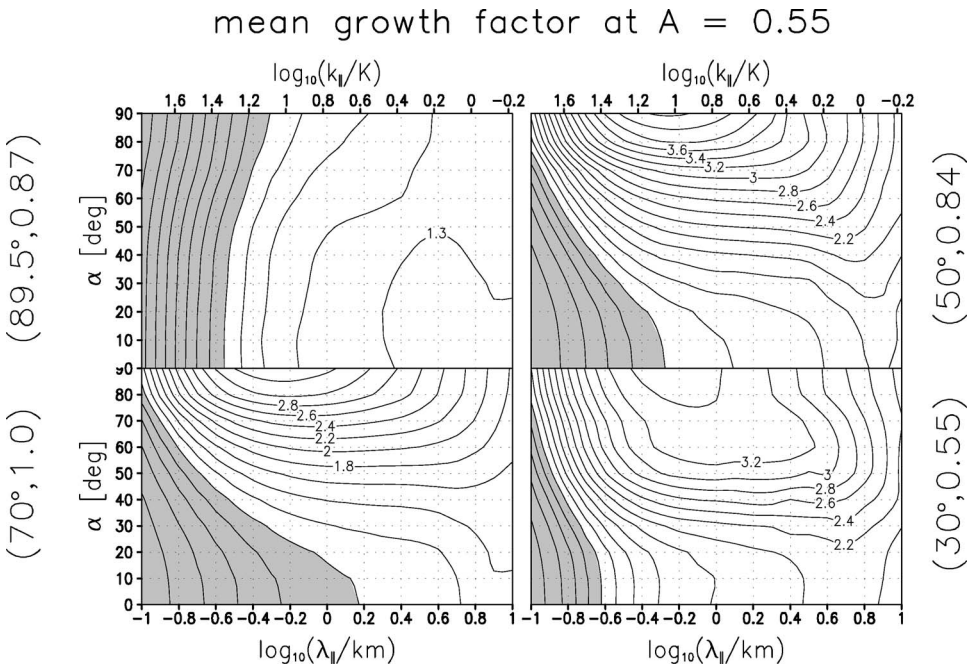

FIG. 28. Similar to Fig. 6, but now showing the mean growth (within 300 s) in the square root of energy from initial random perturbations with a 5/3 power law in the wavenumber in ϕ direction. The contour interval is 0.1 for the IGW case $(\Theta=89.5°)$ and 0.2 everywhere else. Values less than 1 are indicated by shading.

Downloaded 03 Nov 2005 to 195.37.145.100. Redistribution subject to AIP license or copyright, see http://pof.aip.org/pof/copyright.jsp

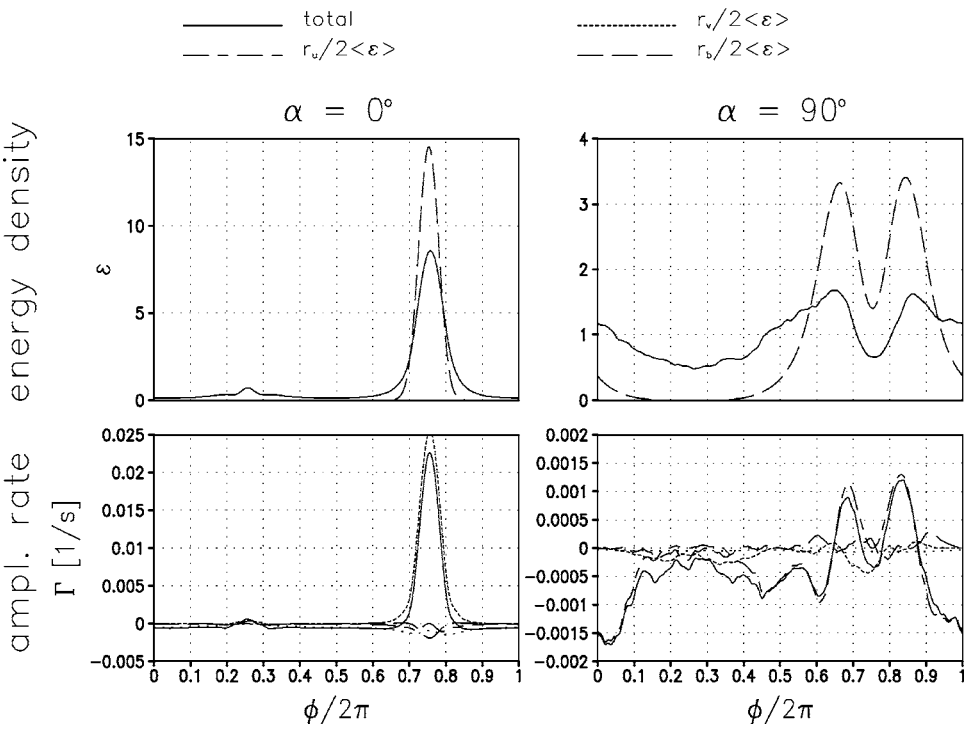

FIG. 29. Corresponding to Fig. 28, the mean energy density (top row) and IGW-phase-dependent amplification-rate decomposition (bottom) at $t=300$ s for parallel and transverse perturbations at the wavelength of the strongest optimal growth for $(\Theta,a)=(89.5°,0.87)$. In the upper panels the mean energy density is indicated by the solid line while the dashed line shows the same field for the corresponding SV. Both are normalized to have a unit IGW-phase average.

28. This is to be compared to Fig. 6. It is not surprising to find that, in comparison to the optimal-growth factors, these mean growth factors are smaller. On the other hand one also finds even mean growth of random perturbations to be possible for the IGW case, although this one does not have a single growing NM. Moreover, in all cases one sees a reasonable reproduction of the dependence of the growth factors on azimuthal angle and horizontal wavelength. So also here the strongest mean growth is observed in the IGW case for parallel perturbations. The HGW cases show transverse perturbations to extract most of the energy from the wave. For $\Theta=70°$ and $\Theta=50°$ this is in agreement with the optimal-growth results. In these cases also the scale of the strongest growth matches quite well that of the strongest optimal growth. In the case $\Theta=30°$ the leading optimal perturbation is at $\alpha=70°$, while the strongest mean growth is found at $\alpha=90°$, but also here one finds a trace of the optimal-growth results in that at the respective azimuthal angle no maximum exists but a plateau which is not found at the other inclination angles. This is to be seen in contrast to Fig. 5, where the corresponding NM growth factors are shown, with no instability in the IGW case, and the strongest growth for parallel perturbations in the HGW cases.

For the IGW case one sees in Fig. 29 for $t=300$ s the mean energy density and amplification-rate decomposition of parallel and transverse perturbations at the wavelength of the strongest optimal growth. A comparison with the energy density of the SV, indicated by the dashed line in the upper row, suggests that many of the features seen can be explained in terms of optimal growth. This is further supported by the fact that NM cannot be used here, since they all decay. For the case $(\Theta,a)=(70°,1)$ the same fields are shown in Fig. 30. For the transverse perturbations once again optimal-perturbation theory seems to give a useful explanation. The energy density is much more strongly peaked near the location of the SV than in the NM (see Fig. 18). The same disparity between NM and mean structures is also found for the HGW-phase-dependent amplification-rate decomposition. On the other hand, the parallel perturbations do not indicate SV behavior. This is probably an effect of the small-scale structure of the corresponding SV (see also Fig. 22 and Appendix 3). By using a source spectrum with suppressed small-scale activity such a perturbation is prevented to appear. Indeed, in a parallel calculation with random initial states with a white spectrum the parallel SV can be identified (not shown).

VII. SUMMARY AND DISCUSSION

In an analysis within the framework of the Boussinesq equations on an f plane optimal perturbations of monochromatic gravity waves have been determined and compared to corresponding NM. The viscous-diffusive parameters have been chosen so as to agree with the conditions in the middle to upper mesosphere (between 70- and 90-km altitude). The identified SVs, able to extract (via a more flexible development of the perturbation structure) over a finite period more energy from the basic wave than a NM, show interesting behavior in several regards.

Firstly, and similar to results in AS12, IGW can support rapid transient growth by several orders of magnitude (in energy) when no NM instability is found. This is the case for IGW slightly below the overturning threshold ($a=0.87$, say), where NM instabilities are prevented by viscous-diffusive effects. For such cases, optimal-perturbation theory suggests, in contrast to the predictions from NM analyses, the possibility of turbulence onset. This is certainly subject to the condition that the ambient perturbations encountered by such

Downloaded 03 Nov 2005 to 195.37.145.100. Redistribution subject to AIP license or copyright, see http://pof.aip.org/pof/copyright.jsp

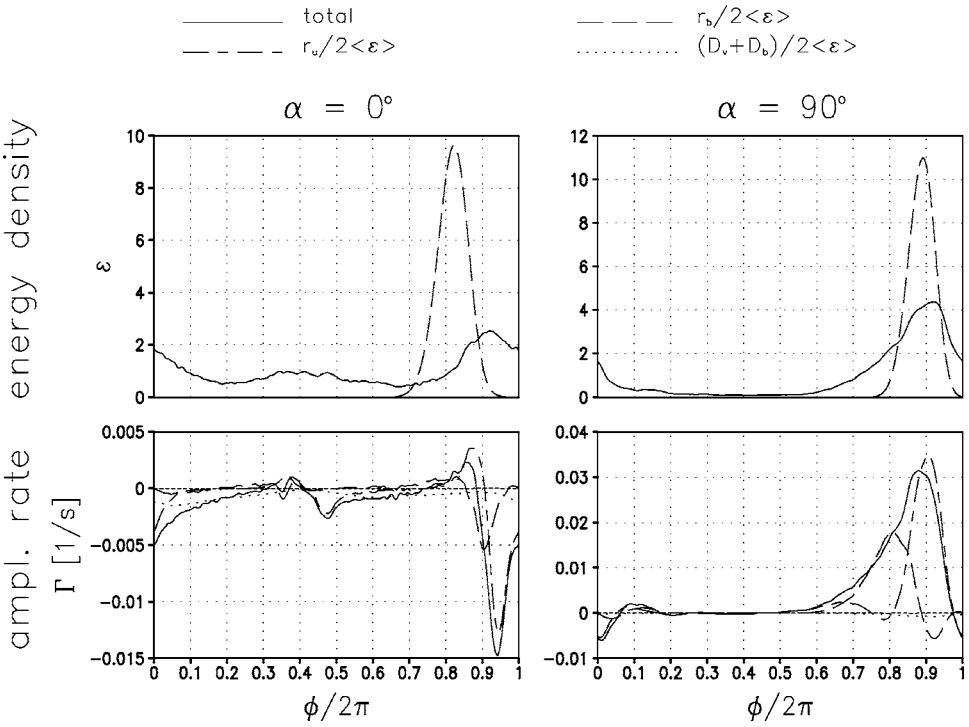

FIG. 30. As Fig. 29, but now for $(\Theta,a)=(70°,1)$.

an IGW are already sufficiently strong so that a further amplitude growth by at most a factor of 20 can lead into a nonlinear development. A possible scenario where this might be relevant could perhaps be an IGW propagating into a region already prepared accordingly by a previous breaking event. As for their structure, the leading SVs are all initially closely confined to the convectively least stable region in the wave. The favored horizontal directions of propagation change from parallel (i.e., in x direction when the IGW propagates in the x-z plane) at optimization times near a Brunt-Vaisala period to transverse (in y direction) at longer times. The dynamics of the SV are characterized by flux-gradient interactions involving the whole circularly polarized velocity field of the IGW, so that simple two-dimensional (2D) approximations of the basic-wave state, e.g., as in a Kelvin-Helmholtz instability, should be seen with caution. Typically SV growth is triggered by convective energy exchange and further sustained by shear-related exchange processes.

Secondly, the leading SVs of all examined HGWs with weak to moderate amplitude, if determined for optimization times shorter than a wave period, show propagation characteristics with respect to the gravity wave, which differ from that of the leading NMs. The latter propagate preferentially in the x-z plane while the former generally favor transverse propagation. Calculations of mean growth from random perturbations indicate just this behavior, which could not be explained with the help of NM.

Thirdly, the leading SVs of the examined HGW differ structurally in an interesting manner from the identified NMs. Initially, they have the form of sharply peaked pulses which are nearly immobile in the geostationary reference frame. In its passage over the SV the HGW repeatedly invigorates the perturbations as they get into contact with suitable buoyancy and velocity gradients in the wave. In the long run the SV structure is often transformed into the broader structure of the leading NM, which moves with the wave phase, but this transition is typically a very long process. Thus, although eventually the leading NMs might take over, SVs highlight the possibility of rapid growth of *local* perturbations, which can get strong enough to initialize turbulence onset *before* the leading broader NM has had time to develop from the SV. As before, this does depend on the specific initial perturbation encountered by a HGW in the real atmosphere (or ocean).

All in all this study seems to support the view that SVs are a relevant factor in the dynamics of turbulence excitation by gravity waves. A conclusive statement, however, is not possible yet. For a full assessment we also need investigations of the nonlinear dynamics of these perturbations, exploring their direct nonlinear behavior as well as secondary instabilities possibly leading to a full three-dimensionalization of the turbulent spectrum. Also the turbulence impact on the basic wave will have to be estimated. It might be that the details of the initial linear dynamics, where the difference between NM and SV is found, do not strongly influence this latter question, but the present study rather seems to suggest that in the interpretation of specific measurements of gravity-wave-excited turbulence optimal perturbations might be helpful, especially as they seem better suited to explain a certain confinement of turbulence to thin layers seen in some observations.[48,49] These also suggest that turbulence in the middle atmosphere often does not coincide with sufficiently small Richardson numbers, which also might be better explainable within the framework of the optimal-perturbation theory. For practical comparison one will have to worry about the perturbation spectrum provided by the ambient fluctuations. Another extension which will be

Downloaded 03 Nov 2005 to 195.37.145.100. Redistribution subject to AIP license or copyright, see http://pof.aip.org/pof/copyright.jsp

necessary at some stage is the introduction of a reference medium with altitude-dependent density. Especially in the atmosphere the Boussinesq equations are bound to reach their limitations as longer time scales are considered in which a gravity wave covers more than one scale height. This might be most relevant for the faster high-frequency gravity waves.

ACKNOWLEDGMENT

The author gratefully acknowledges the helpful comments by G. Schmitz.

APPENDIX: WKB THEORY FOR THE EXPLANATION OF THE TIME DEPENDENCE OF THE SV SCALES

To a large degree, the time dependence of the scales in the various SVs discussed in the main text can be understood on the basis of a standard WKB theory.[4,50] This appendix first describes the theory in general and then gives the applications.

1. General theory

The WKB theory assumes that the spatial scale over which the wavelength of the SV varies is comparatively long. The same holds for the time scale describing variations of the period of the oscillations within the SV. One thus uses the ansatz

$$\begin{pmatrix} \mathbf{v} \\ b \end{pmatrix}(\phi,t) = \begin{pmatrix} \tilde{\mathbf{v}} \\ \tilde{b} \end{pmatrix}(\epsilon\phi,\epsilon t)e^{i\chi(\epsilon\phi,\epsilon t)/\epsilon}, \tag{A1}$$

where $\epsilon \ll 1$ is a slowness parameter and χ the local phase of the wave packet. One then introduces the slow spatial and time coordinates $\Phi=\epsilon\phi$ and $T=\epsilon t$, defines the local frequency $\omega=-\partial\chi/\partial T$ and the local wavenumber $\mu=K\partial\chi/\partial\Phi$, and inserts (A1) into (17)–(21). Assuming the gravity-wave fields also only to depend on Φ, i.e., to be slowly dependent on the phase, and neglecting rotation, viscosity, and diffusion one finds to lowest order in ϵ the WKB dispersion relation

$$\omega(\Phi,T) = \tilde{\omega}[\mu(\Phi,T),\Phi] = U_\xi\kappa + V\lambda - \frac{\Omega}{K}\mu \pm N_{\mathrm{tot}}\sqrt{\frac{\lambda^2+(\kappa\sin\Theta+\mu\cos\Theta)^2}{\kappa^2+\lambda^2+\mu^2}}, \tag{A2}$$

which simply is the dispersion relation for gravity waves in a constant background flow without rotation, but with modified static stability $N_{\mathrm{tot}}^2=N^2+\partial B/\partial z$, in the special rotated and translated reference system used throughout this study. Since $\partial\mu/\partial T=-K\partial\omega/\partial\Phi$ (A2) also gives rise to the eikonal equations

$$\left(\frac{\partial}{\partial T}+c_g K\frac{\partial}{\partial\Phi}\right)\omega = 0, \tag{A3}$$

$$\left(\frac{\partial}{\partial T}+c_g K\frac{\partial}{\partial\Phi}\right)\mu = -K\frac{\partial\tilde{\omega}}{\partial\Phi}, \tag{A4}$$

where $c_g=\partial\tilde{\omega}/\partial\mu$ is the group velocity of the perturbation. Along rays defined by this group velocity the frequency is therefore a conserved quantity, so that for any frequency the wavenumber μ can be calculated from (A2) as a function of ϕ.

2. Optimal perturbations of IGW

In the case of the SV for IGW one can use that, as shown by AS12, the frequency of the developing optimal perturbations is determined to a good approximation by the advection of the perturbation in its direction of propagation by the corresponding horizontal flow-field component at the statically least stable location $\phi=3\pi/2$, i.e., $\omega=U_\xi(\phi=3\pi/2)\kappa$ (since V vanishes at this location). In addition, the phase velocity of the IGW Ω/K is very small, so that it can be neglected in (A2).

Assuming also $\cos\Theta=0$ and $\sin\Theta=1$, one finds for *parallel* SV, where $\lambda=0$, and assuming $\kappa>0$,

$$\frac{U_\xi(3\pi/2)-U_\xi}{N_{\mathrm{tot}}/\kappa} = \pm\frac{1}{\sqrt{1+\mu^2/\kappa^2}}. \tag{A5}$$

Obviously, since the left-hand side is always negative (for $a<1$), only the branch with the minus sign in front of the square root (the branch with upwards pointing group velocity at $\mu>0$) can satisfy this equation. Note that, the nearer one is to the maximum of U_ξ at $\phi=\pi/2$, the smaller μ must be, so that near this location the vertical wavelength in the SV gets largest. Moreover, propagation through $\phi=\pi/2$ is only possible if there

$$1 > \frac{U_\xi - U_\xi(3\pi/2)}{N_{\mathrm{tot}}/\kappa} = \frac{4A}{\sqrt{1+a}}\frac{\kappa}{K}. \tag{A6}$$

Radiation is thus only possible for κ small enough. At $A=0.55$, and thus $a=0.87$, this is neither the case for the parallel SV for $\tau=5$ min, where $\kappa/K=9.5$, nor for the parallel SV for $\tau=30$ min, where $\kappa/K=0.76$. In the latter case, however, one is nearer to the radiation condition, so that energy can move close to $\phi=\pi/2$, explaining the near-vertical structures at $\phi=\pi/2$ in Fig. 17. For this case Fig. 31 also shows the distribution of frequency and group velocity according to (A2) in the (μ,ϕ) plane. One also sees there that rays with $\omega=U_\xi(\phi=3\pi/2)\kappa\approx-0.167$ cannot propagate through $\phi=\pi/2$ but get progressively larger in scale (i.e., smaller in μ) as they approach this location.

Similarly one derives for *transverse* SV, where $\kappa=0$, and assuming $\lambda>0$,

$$-\frac{V\lambda}{N_{\mathrm{tot}}} = \pm\frac{1}{\sqrt{1+\mu^2/\lambda^2}}. \tag{A7}$$

One sees directly that near the zero lines of V, i.e., at $\phi=\pi/2,3\pi/2$, the vertical scale of the SV collapses (i.e., $\mu\to\infty$), leading to the critical-layer behavior visible for all transverse SVs of the IGW. Without neglect of the IGW-phase velocity the divergence of μ is modified to a develop-

Downloaded 03 Nov 2005 to 195.37.145.100. Redistribution subject to AIP license or copyright, see http://pof.aip.org/pof/copyright.jsp

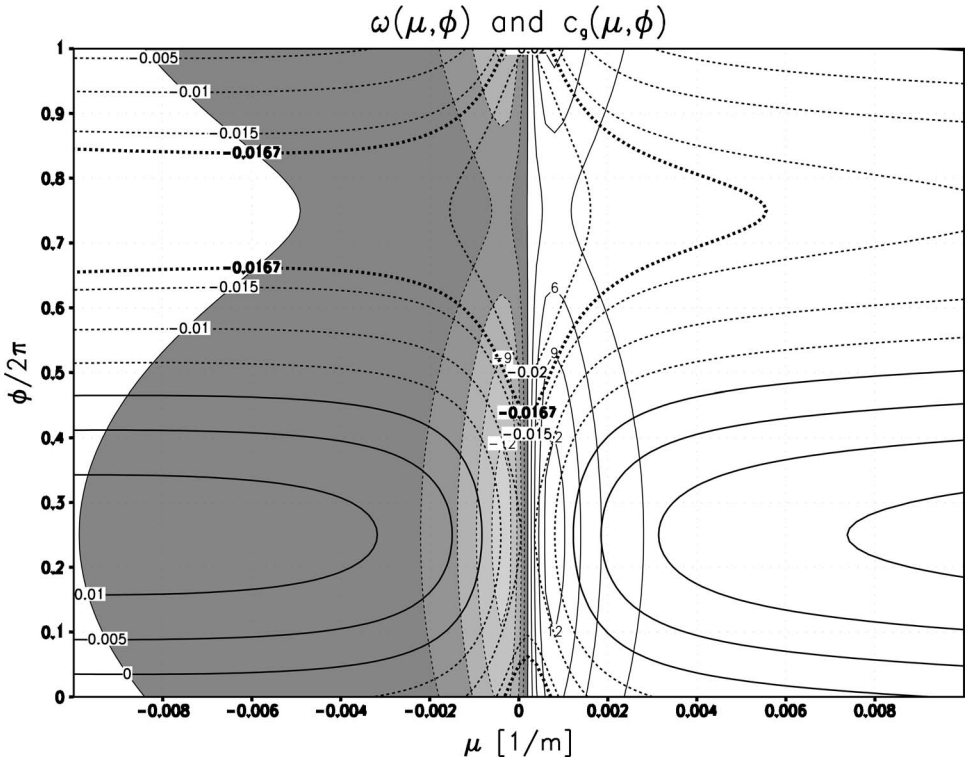

FIG. 31. For parallel SV of the subcritical IGW ($\Theta=89.5°$) with $A=0.55$ and $a=0.87$, the dependence of frequency (thick contours) and group velocity (thin contours, negative values indicated by shading) according to the WKB theory on the IGW-phase ϕ and the wavenumber μ in phase direction. The isoline corresponding to the parallel SV for $\tau=30$ min, where $\omega\approx -0.0167$, is drawn extra fat. The movement of a ray is along the isolines of constant frequency, while the velocity in ϕ direction is given by the group velocity.

ment towards finite large wavenumbers,[51] but the basic effect remains as described.

3. Scale oscillation of parallel singular vectors in high-frequency gravity waves

The oscillation between weak and strong viscous and diffusive damping for the leading parallel SV for high-frequency gravity waves, e.g., visible for $(\Theta,a)=(70°,1)$ in Figs. 19 and 23, is due to an oscillation of the scale of this perturbation in ϕ direction which can be seen in Fig. 22. It has the shape of a nearly monochromatic wave packet with a wavelength which, consistent with the observed time dependence of the viscous and diffusive losses, is especially small when it passes $\phi=\pi/2$ and which maximizes as the SV is near $\phi=3\pi/2$. Also this behavior can be explained using the WKB theory.

Since the SV moves approximately with the negative phase velocity of the gravity wave, i.e., $c_g\approx-\Omega/K$, the square root in (A2), i.e., the intrinsic-frequency contribution, can be neglected, yielding

$$\mu = K(U_\xi\kappa-\omega)/\Omega, \tag{A8}$$

since for parallel perturbations $\lambda=0$. The spatial dependence of μ thus results from that of U_ξ.

For a test whether (A8) actually describes the scale behavior of the parallel SV shown in Fig. 32 $\mu(\phi,t)$ has been determined diagnostically by minimizing

$$C(\mu) = \left| K\frac{\partial}{\partial\phi}\begin{pmatrix}\mathbf{v}\\ b\end{pmatrix} - i\mu\begin{pmatrix}\mathbf{v}\\ b\end{pmatrix}\right|^2. \tag{A9}$$

Figure 32 shows the result, agreeing quite well with the qualitative expectation of small μ near $\phi=3\pi/2$ and large μ near $\phi=\pi/2$. In the same manner one also could have determined the frequency ω from time derivatives. It turns out,

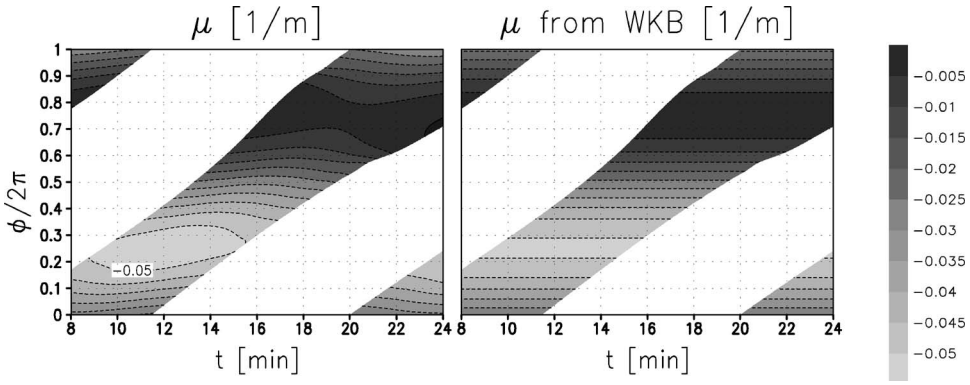

FIG. 32. Time dependence in the wavenumber μ in ϕ direction in the subcycle of the parallel SV for the gravity wave with $(\Theta,a)=(70°,1)$ also shown in Fig. 23, as diagnosed from the data of the linear model (left) or predicted from the WKB theory (right). The shading scale is defined in the shading bar.

Downloaded 03 Nov 2005 to 195.37.145.100. Redistribution subject to AIP license or copyright, see http://pof.aip.org/pof/copyright.jsp

however, that the time oscillation in all fields is so regular that one can just count peaks, which gave a single period of about 35 s. This has been inserted into (A8), yielding the predicted wavenumber also shown in Fig. 32.

[1] D. C. Fritts and M. J. Alexander, "Gravity wave dynamics and effects in the middle atmosphere," Rev. Geophys. **41**, 1003 (2003).
[2] P. Müller, G. Holloway, F. Henyey, and N. Pomphrey, "Nonlinear interactions among internal gravity waves," Rev. Geophys. **24**, 493 (1986).
[3] C. O. Hines, "Internal atmospheric gravity waves at ionospheric heights," Can. J. Phys. **38**, 1441 (1960).
[4] F. P. Bretherton, "The propagation of groups of internal gravity waves in a shear flow," Q. J. R. Meteorol. Soc. **92**, 466 (1966).
[5] J. R. Booker and F. P. Bretherton, "The critical layer for internal gravity waves in a shear flow," J. Fluid Mech. **27**, 513 (1967).
[6] R. S. Lindzen, "Turbulence and stress owing to gravity wave and tidal breakdown," J. Geophys. Res. **86**, 9707 (1981).
[7] F.-J. Lübken, "Seasonal variation of turbulent energy dissipation rates at high latitudes as determined by *in situ* measurements of neutral density fluctuations," J. Geophys. Res. **102**, 13441 (1997).
[8] A. S. Medvedev and G. P. Klaassen, "Vertical evolution of gravity wave spectra and the parameterization of associated gravity wave drag," J. Geophys. Res. **100**, 25841 (1995).
[9] C. O. Hines, "Doppler spread parameterization of gravity-wave momentum deposition in the middle atmosphere. Part 1. Basic formulation," J. Atmos. Sol.-Terr. Phys. **59**, 371 (1997).
[10] C. O. Hines, "Doppler spread parameterization of gravity-wave momentum deposition in the middle atmosphere. Part 2. Broad spectra and quasi-monochromatic spectra and implementation," J. Atmos. Sol.-Terr. Phys. **59**, 387 (1997).
[11] M. J. Alexander and T. J. Dunkerton, "A spectral parameterization of mean-flow forcing due to breaking gravity waves," J. Atmos. Sci. **56**, 4167 (1999).
[12] C. D. Warner and M. E. McIntyre, "An ultra-simple spectral parameterization for non-orographic gravity waves," J. Atmos. Sci. **58**, 1837 (2001).
[13] K. B. Winters and E. A. D'Asaro, "Three-dimensional wave instability near a critical level," J. Fluid Mech. **272**, 255 (1994).
[14] Ø. Andreassen, C. E. Wasberg, D. C. Fritts, and J. R. Isler, "Gravity wave breaking in two and three dimensions. 1. Model description and comparison of two-dimensional evolutions," J. Geophys. Res. **99**, 8095 (1994).
[15] D. C. Fritts, J. R. Isler and Ø. Andreassen, "Gravity wave breaking in two and three dimensions. 2. Three-dimensional evolution and instability structure," J. Geophys. Res. **99**, 8109 (1994).
[16] J. R. Isler, D. C. Fritts, Ø. Andreassen, and C. E. Wasberg, "Gravity wave breaking in two and three dimensions. 3. Vortex breakdown and transition to isotropy," J. Geophys. Res. **99**, 8125 (1994).
[17] M. P. Lelong and T. J. Dunkerton, "Inertia-gravity wave breaking in three dimensions. Part I. Convectively stable waves," J. Atmos. Sci. **55**, 2473 (1998).
[18] M. P. Lelong and T. J. Dunkerton, "Inertia-gravity wave breaking in three dimensions. Part II. Convectively unstable waves," J. Atmos. Sci. **55**, 2489 (1998).
[19] J. A. Werne and D. C. Fritts, "Stratified shear turbulence: Evolution and statistics," Geophys. Res. Lett. **26**, 439 (1999).
[20] D. C. Fritts, C. Bizon, J. A. Werne, and C. K. Meyer, "Layering accompanying turbulence generation due to shear instability and gravity-wave breaking," J. Geophys. Res. **108**, 8452 (2003).
[21] L. Howard, "A note on a paper of J. W. Miles," J. Fluid Mech. **10**, 509 (1961).
[22] J. W. Miles, "On the stability of heterogeneous shear flows," J. Fluid Mech. **10**, 496 (1961).
[23] R. P. Mied, "The occurrence of parametric instabilities in finite amplitude internal gravity waves," J. Fluid Mech. **78**, 763 (1976).
[24] J. Klostermeyer, "On parametric instabilities of finite-amplitude internal gravity waves," J. Fluid Mech. **119**, 367 (1982).
[25] J. Klostermeyer, "Parametric instabilities of internal gravity waves in Boussinesq fluids with large Reynolds numbers," Geophys. Astrophys. Fluid Dyn. **26**, 85 (1983).
[26] J. Klostermeyer, "Two- and three-dimensional parametric instabilities in finite amplitude internal gravity waves," Geophys. Astrophys. Fluid Dyn. **61**, 1 (1991).
[27] P. N. Lombard and J. R. Riley, "Instability and breakdown of internal gravity waves. I. Linear stability analysis," Phys. Fluids **8**, 3271 (1996).
[28] L. J. Sonmor and G. P. Klaassen, "Toward a unified theory of gravity wave stability," J. Atmos. Sci. **54**, 2655 (1997).
[29] D. C. Fritts and L. Yuan, "Stability analysis of inertio-gravity wave structure in the middle atmosphere," J. Atmos. Sci. **46**, 1738 (1989).
[30] L. Yuan and D. C. Fritts, "Influence of a mean shear on the dynamical instability of an inertio-gravity wave," J. Atmos. Sci. **46**, 2562 (1989).
[31] T. J. Dunkerton, "Shear instability of internal inertia-gravity waves," J. Atmos. Sci. **54**, 1628 (1997).
[32] F. Kwasniok and G. Schmitz, "Radiating instabilities of internal inertio-gravity waves," J. Atmos. Sci. **60**, 1257 (2003).
[33] K.-H. Yau, G. P. Klaassen, and L. J. Sonmor, "Principal instabilities of large amplitude inertio-gravity waves," Phys. Fluids **16**, 936 (2004).
[34] B. F. Farrell, "Optimal excitation of neutral Rossby waves," J. Atmos. Sci. **45**, 163 (1988).
[35] B. F. Farrell, "Optimal excitation of perturbations in viscous shear," Phys. Fluids **31**, 2093 (1988).
[36] L. Boberg and U. Brosa, "Onset of turbulence in a pipe," Z. Naturforsch., A: Phys. Sci. **43**, 697 (1988).
[37] K. M. Butler and B. F. Farrell, "Three dimensional optimal perturbations in viscous shear flow," Phys. Fluids A **4**, 1637 (1992).
[38] L. N. Trefethen, A. E. Trefethen, S. C. Reddy, and T. A. Driscoll, "Hydrodynamic stability without eigenvalues," Science **261**, 578 (1993).
[39] U. Achatz and G. Schmitz, "Shear and static instability of inertia-gravity wave packets: Short-term modal and nonmodal growth," J. Atmos. Sci. (to be published).
[40] U. Achatz and G. Schmitz, "Optimal growth in inertia-gravity wave packets: Energetics, long-term development, and three-dimensional structure," J. Atmos. Sci. (to be published).
[41] P. G. Drazin, "On the instability of an internal gravity wave," Proc. R. Soc. London, Ser. A **356**, 411 (1977).
[42] D. C. Fritts and P. K. Rastogi, "Convective and dynamical instabilities due to gravity wave motions in the lower and middle atmosphere: Theory and observations," Radio Sci. **20**, 1247 (1985).
[43] C. M. Bender and S. A. Orszag, *Advanced Mathematical Methods for Scientists and Engineers* (McGraw-Hill, New York, 1978).
[44] D. R. Durran, *Numerical Methods for Wave Equations in Geophysical Fluid Dynamics* (Springer, New York 1999).
[45] R. B. Lehoucq, D. C. Sorensen, and C. Yang, ARPACK users' guide: Solution of large-scale eigenvalue problems with implicitly restarted Arnoldi methods, SIAM, Philadelphia, PA, 1998.
[46] R. Giering and T. Kaminski, "Recipes for adjoint code construction," ACM Trans. Math. Softw. **24**, 437 (1998).
[47] F. Lott, "The transient emission of propagating gravity waves by a stably stratified shear layer," Q. J. R. Meteorol. Soc. **123**, 1603 (1997).
[48] A. Müllemann, M. Rapp, and F.-J. Lübken, "Morphology of turbulence in the polar summer mesopause region during the MIDAS/SOLSTICE campaign 2001," Adv. Space Res. **31**, 2069 (2003).
[49] B. Strelnikov, M. Rapp, and F.-J. Lübken, "A new technique for the analysis of neutral air density fluctuations measured *in situ* in the middle atmosphere," Geophys. Res. Lett. **30**, 2052 (2003).
[50] F. P. Bretherton, "The general linearized theory of wave propagation," Lect. Appl. Math. **13**, 61 (1971).
[51] D. Broutman and W. R. Young, "On the interaction of small-scale oceanic internal waves with near-inertial waves," J. Fluid Mech. **166**, 341 (1986).

Downloaded 03 Nov 2005 to 195.37.145.100. Redistribution subject to AIP license or copyright, see http://pof.aip.org/pof/copyright.jsp